Cationic-π Interactions enabling Hard/Soft Ti/Ag Heterobimetallic Cooperativity in Lactide Ring-Opening Polymerisation

Chloe A. Baker, Charles Romain*, Nicholas J. Long*

Department of Chemistry, Imperial College London, Molecular Sciences Research Hub, White City Campus, Wood Lane, London, W12 0BZ, UK.

FAIR data are available at DOI: 10.14469/hpc/8729, as per funding council guidance.[1]

Index

General Methods:

All synthetic manipulations were carried out using an inert atmosphere of dry nitrogen using standard Schlenk and glovebox techniques. Hexane, toluene and DCM were obtained from MBraun MB-SPS 800 solvent towers and stored over 3Å molecular sieves and degassed for 1 hour. THF was distilled from sodium/benzophenone under dry nitrogen, stored over 3Å molecular sieves, and degassed for 1 hour. Deuterated benzene and chloroform were distilled from CaH_2, degassed by several freeze-pump-thaw cycles and stored over 3Å molecular sieves. The salen pro-ligand ^{H2}**L** was synthesised following a standard literature procedure using ethylenediamine and 3,5,-di-*tert*-butyl salicyaldehyde.[2] *Rac*-lactide (*rac*-LA) was recrystallised from dry toluene ([*rac*-LA]$_0$ = 1 M at 90 ^{o}C) and sublimed three times under reduced pressure. AgBArF was prepared from a known literature procedure via salt metathesis using NaBArF and $AgNO_3$.[3] All other reagents were obtained from commercial sources and used as received.

Characterisation Methods:

NMR spectra were recorded on Bruker Av400 at 298 K unless specified. All chemical shifts were determined using residual signals of the deuterated solvents were calibrated vs $SiMe_4$.

Gel permeation chromatography (GPC) was performed using Agilent 1260 Infinity II Multi-Detector GPC System with Agilent PLgel 5µm MIXED-C 300 x 7.5 mm columns, calibrated using a polystyrene standard with THF as eluent at a 1 mL min^{-1} flow rate. Polymer samples were dissolved in GPC grade THF and filtered prior to analysis.

MALDI-ToF mass spectrometry measurements were performed on Waters/Micromass MALDI micro MX spectrometer with MassLynx Mass Spectrometry Software using positive ionisation. Polymers were dissolved in THF at a concentration of 10 mg mL^{-1}. Dithranol was used as a matrix (10 mg mL^{-1} in THF). Potassium trifluoroacetate (KTFA) was used as cationising agent (| 10 mg mL^{-1} in THF). The solutions of polymer, matrix and salt were mixed in a ratio of 1/1/1 (v/v/v), respectively. The mixed solution was spotted on a stainless steel MALDI plate and left to dry for a couple of hours. The spectra were recorded using reflectron mode. Data were analysed using mMass[3] and considering the monoisotopic masses.[4]

UV-Visible absorption spectra were measured using an Agilent Technologies Cary 60 Spectrophotometer operating with WinUV software. The sample was held in a quartz cuvette sealed under an inert atmosphere at a path length of 1 cm. Absorption spectra were recorded against a baseline of pure solvent (DCM), with a scan rate of 600 nm min^{-1} and a data interval of 1.0 nm. Solutions were prepared at c = 100 µM in DCM.

General Polymerisation Procedure:

- *For reactions at room temperature:*

In a glovebox, to solution of *rac*-LA/DCM (144 mg, 1 mmol, 1.0 M, 100 eq) in a PTFE screw-capped vial, stock solutions of catalyst/dcm (6.6 mg, 10 µmol, 1 eq) and AgBArF/dcm (9.7 mg, 10 µmol, 1 eq) were added. DCM was added to lactide prior to the stock solutions, so the overall final concentration is [LA] = 1.0 M). The vial was capped and stirred at room temperature in the glovebox. An aliquot was taken by taking 100 µL of solution and quenching in 300 µL hexane.

- *For reactions at 90 ^{o}C:*

Same procedure as above but toluene was exclusively used as solvent. *Rac*-LA was weighted in a vial then toluene was added so [LA] = 1 M after addition of the stock solutions of catalysts. The vials were taken from the glovebox and set into a pre-heated dry syn, and in this case the reactivity was quenched by exposure to air. Integration of the methine protons in the ^{1}H NMR spectrum allowed conversion to be determined. The polymer could be precipitated using methanol.

Complex synthesis and characterisation:

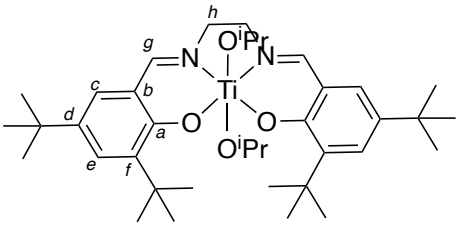

Synthesis of **1**:[5] To a solution of ^{2H}L (200 mg, 0.406 mmol, 1.0 equiv.) in toluene (4 mL) a solution of Ti(O^{i}Pr)$_4$ (115 mg, 0.406 mmol, 1.0 equiv.) in toluene (1 mL) was added, and left to stir at room temperature overnight. The solvent was removed *in vacuo* and resulting yellow solid washed in cold hexane and isolated via centrifugation. The resulting yellow solid was dried under high vacuum for 2 hours. (235 mg, 0.358 mmol, 88 %).

^{1}H NMR: (400 MHz, $CDCl_3$, δ (ppm)): 8.27 (s, 2H, *H*C=N) 7.48 (d, 2H, *H*C$^{c/e}$, $^4J_{HH}$ = 2.5 Hz) 7.16 (d, 2H, *H*C$^{c/e}$, $^4J_{HH}$ = 2.5 Hz) 4.13 (hep, 2H, OC*H*(CH$_3$)$_2$, $^3J_{HH}$ = 6.1 Hz), 3.96 (s, 4H, C*H*$_2$), 1.49 (s, 18H, C(C*H*$_3$)$_3$) 1.32 (s, 18H, C(C*H*$_3$)$_3$), 0.66 (d, 12H, OCH(C*H*$_3$)$_2$, $^3J_{HH}$ = 6.0 Hz). **^{13}C{^{1}H}^{6} NMR** (101 MHz, $CDCl_3$, δ (ppm)): 163.6 (*C*^{a}), 163.5 (H*C*=N), 138.3 (*C*$^{d/f}$), 137.3 (*C*$^{d/f}$), 129.9 (*C*$^{c/e}$), 127.7 (*C*$^{c/e}$), 122.0 (*C*^{b}), 72.6 (O*C*H(CH$_3$)$_2$), 58.6 (*C*H$_2$), 35.6 (C$^{f/d}$*C*(CH$_3$)$_3$), 34.2 (C$^{f/d}$*C*(CH$_3$)$_3$), 31.1 (C$^{f/d}$C(*C*H$_3$)$_3$), 29.8(C$^{f/d}$C(*C*H$_3$)$_3$), 26.0 (OCH(*C*H$_3$)$_2$). **EA** for $C_{38}H_{60}N_2O_4Ti$. Expected: C, 69.49; H, 9.21; N, 4.27. Found: C, 68.85; H, 8.74; N, 4.97.

***In-situ* characterisation:**

1 (1 equiv.) +**AgBArF** (1 equiv) in C_6D_6:

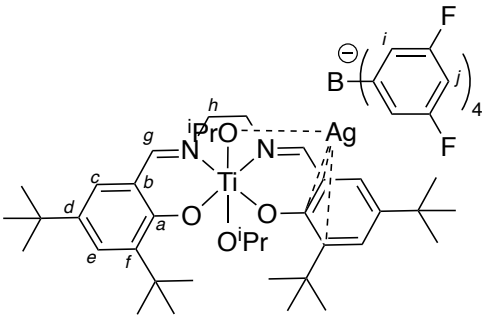

^{1}H NMR (400 MHz, C_6D_6): 8.40 (s, 8H, C^i*H*), 7.70 (d, 2H, C$^{c/e}$, $^4J_{HH}$ = 2.4 Hz), 7.69 (s, 4H, C^j*H*), 7.65 (s, 2H, N=C*H*), 7.24 (d, 2H, C$^{c/e}$, $^4J_{HH}$ = 2.4 Hz), 3.91 (m, 1H, C*H*(CH$_3$)$_2$), 3.56 (m, 1H, C*H*(CH$_3$)$_2$), 3.15-3.20 (br m, 4H, CH$_2$), 1.53 (s, 18H, C*H*$_3$), 1.28 (s, 18H, C*H*$_3$), 0.48 (br m, 6H, CH(C*H*$_3$)$_2$), 0.30 (br m, 6H, CH(C*H*$_3$)$_2$). **^{13}C NMR** (101 MHz, C_6D_6): 164.7 (*C*^{a}), 160.6 (*C*=N), 142.9 (*C*$^{d/f}$), 137.8 (*C*$^{d/f}$), 135.5 (*C*^{i}), 131.8 (*C*$^{c/e}$), 128.5 (*C*$^{c/e}$) 126.6 (*C*-F), 123.9 (*C*-B), 122.0 (*C*^{b}), 117.8 (*C*^{j}) 65.9 (diethyl ether), 57.9 (*C*H$_2$) 35.8 (*C*(CH$_3$)$_3$), 34.4 (*C*(CH$_3$)3), 31.3 C(*C*H$_3$)$_3$), 30.1 (C(*C*H$_3$)$_3$), 24.1 (CH(*C*H$_3$)$_2$), 24.3(CH(*C*H$_3$)$_2$), 15.6 (diethyl ether).

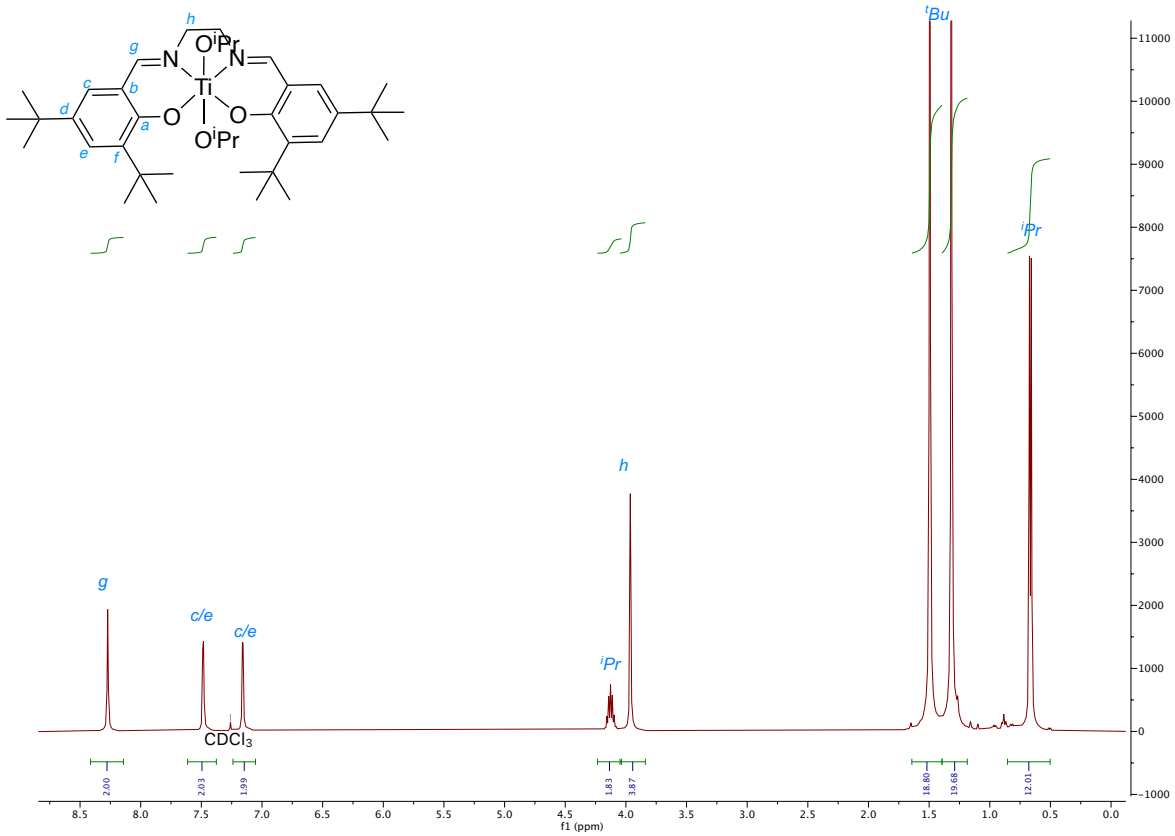

Figure S1: ^{1}H NMR (400 MHz, $CDCl_3$) for **1** (data available at DOI: 10.14469/hpc/8765).

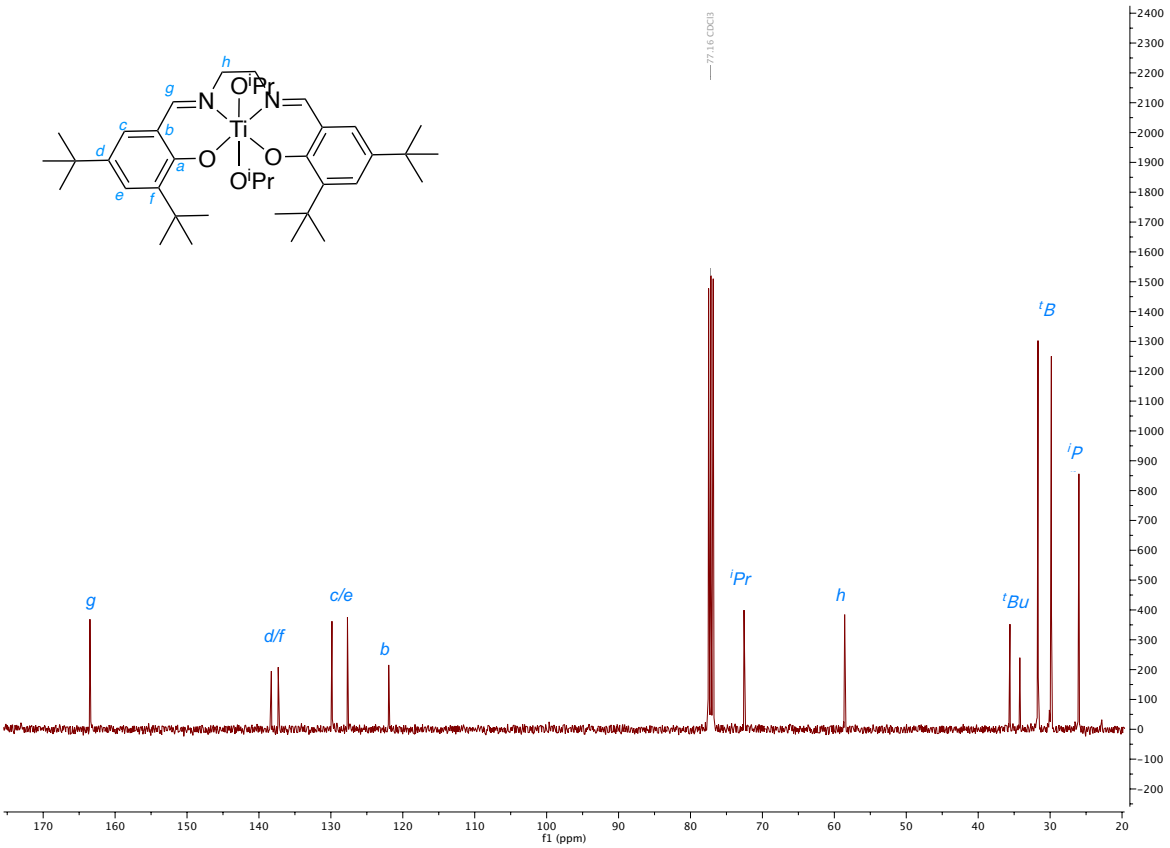

Figure S2: ^{13}C NMR spectrum (101 MHz, $CDCl_3$) for **1** (data available at DOI: 10.14469/hpc/8765).

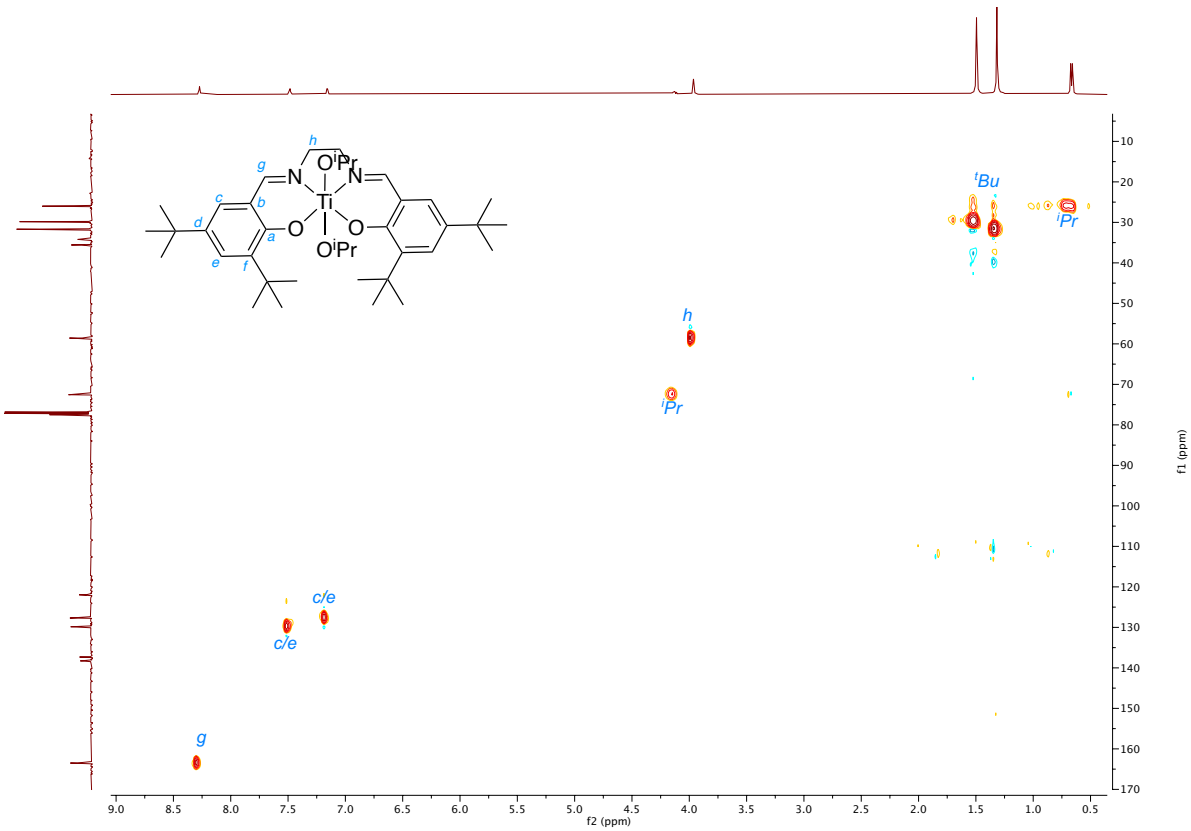

Figure S3: {^{1}H-^{13}C}-HSQC ($CDCl_3$) NMR spectrum for **1** (data available at DOI: 10.14469/hpc/8765).

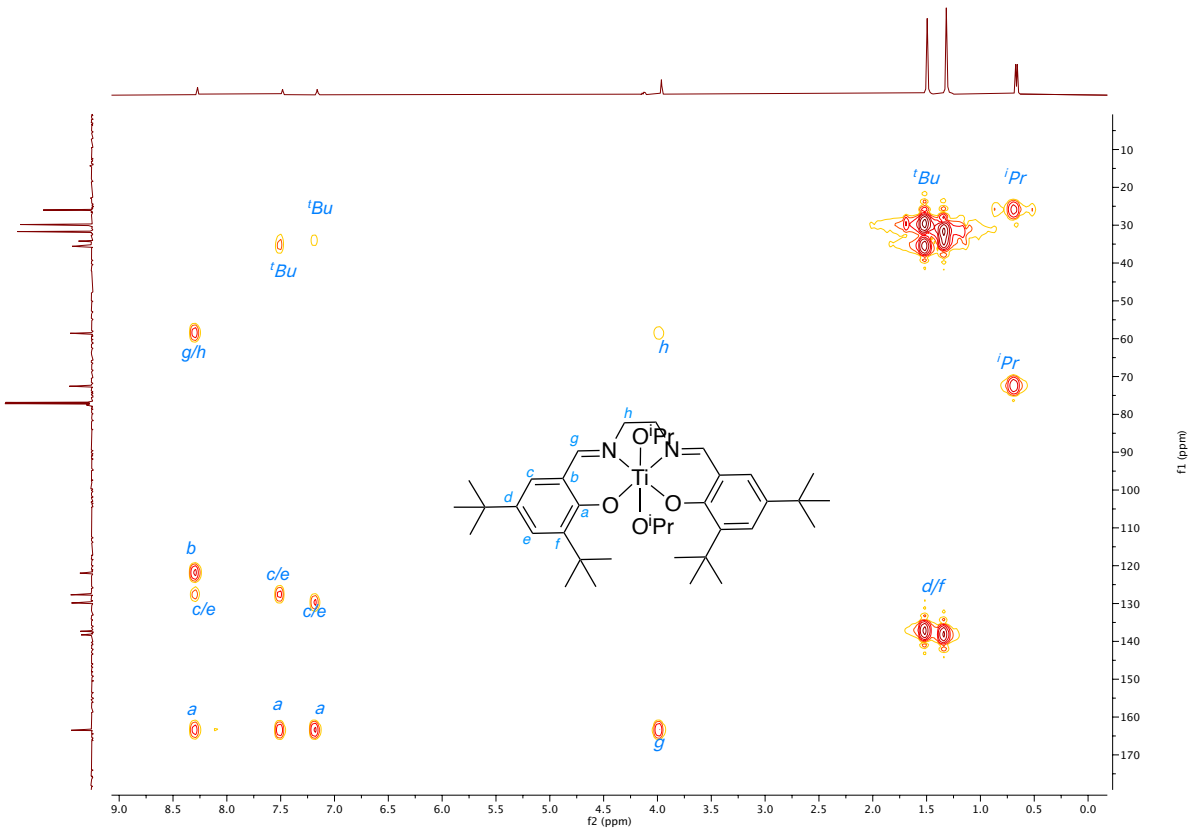

Figure S4: {^{1}H-^{13}C}-HMBC spectrum ($CDCl_3$) for **1** (data available at DOI: 10.14469/hpc/8765).

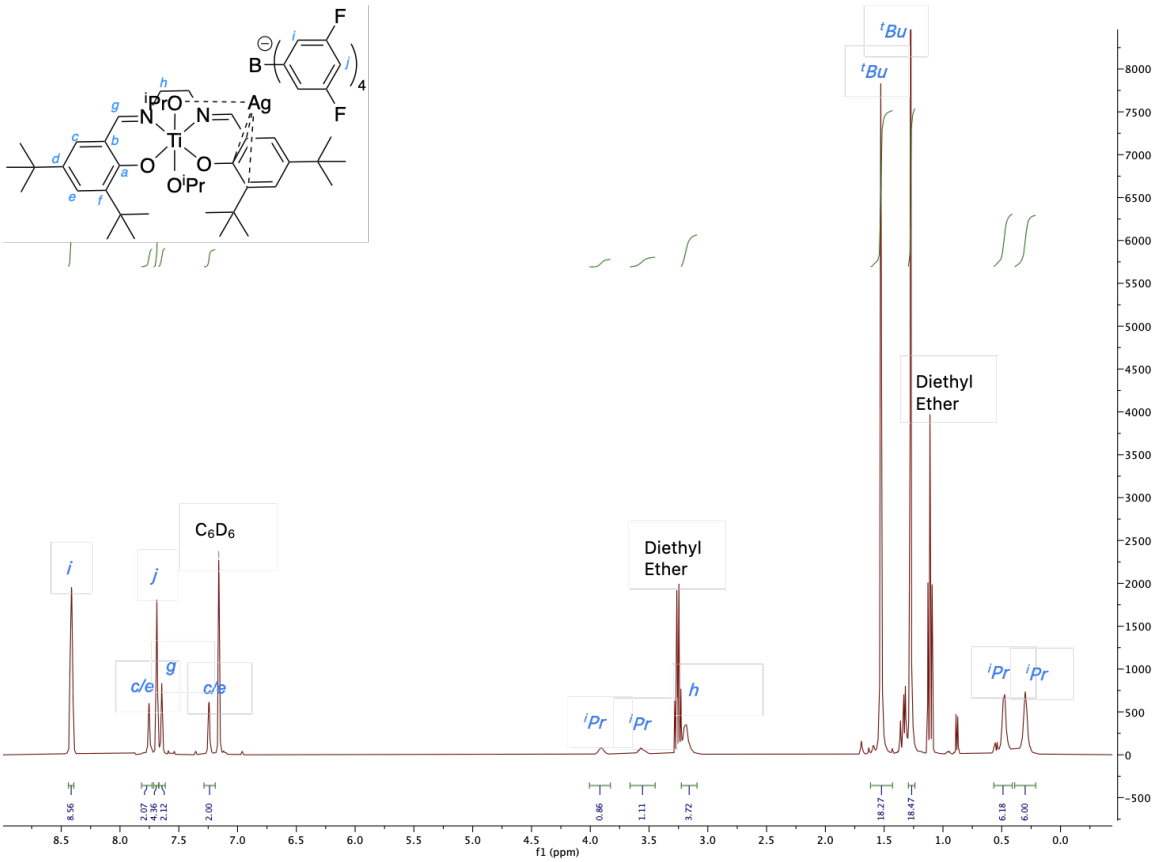

Figure S5: ^{1}H NMR spectrum of **1-AgBArF** *in-situ* generated by addition of equimolar AgBArF to **1** in C_6D_6 (data available at DOI: 10.14469/hpc/9854)

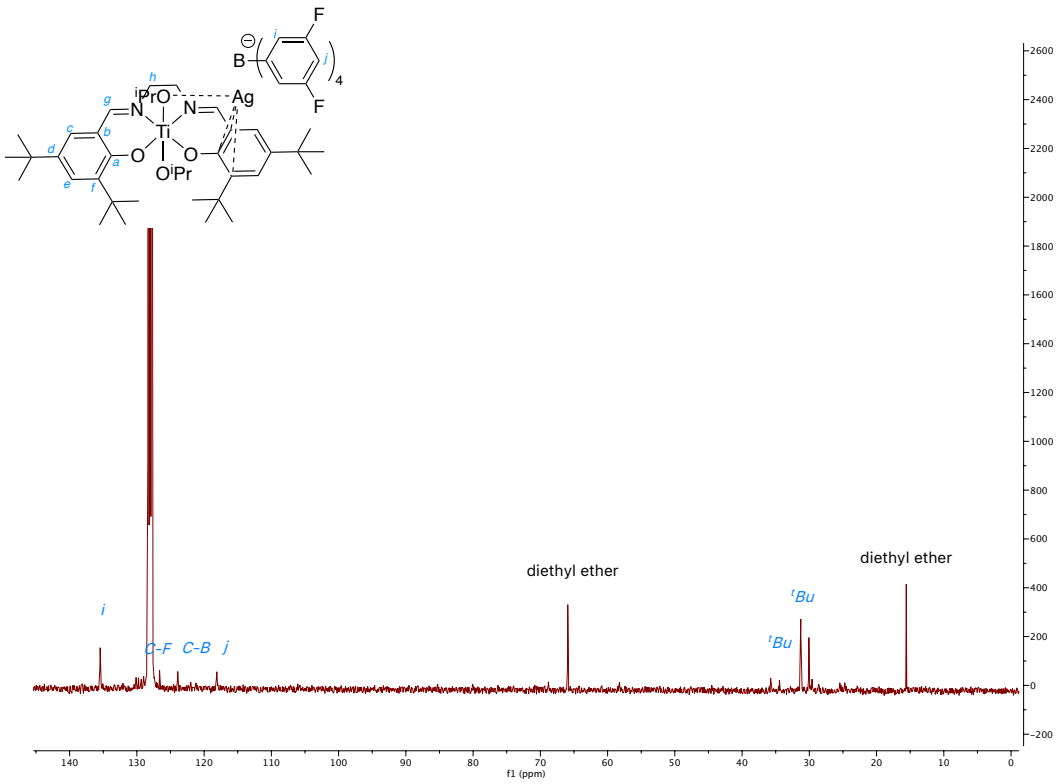

Figure S6: ^{13}C NMR spectrum of **1-AgBArF** *in-situ* generated by addition of equimolar AgBArF to **1** in C_6D_6.

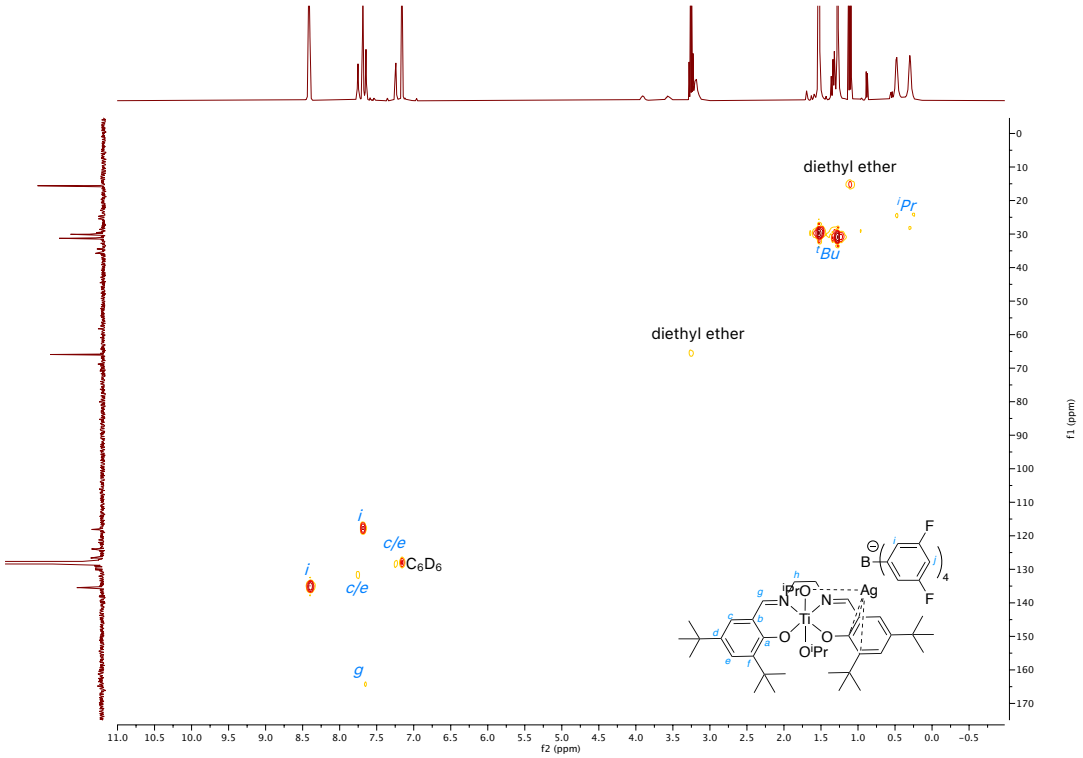

Figure S7: HSQC NMR spectrum of **1-AgBArF** *in-situ* generated by addition of equimolar AgBArF to **1** in C_6D_6.

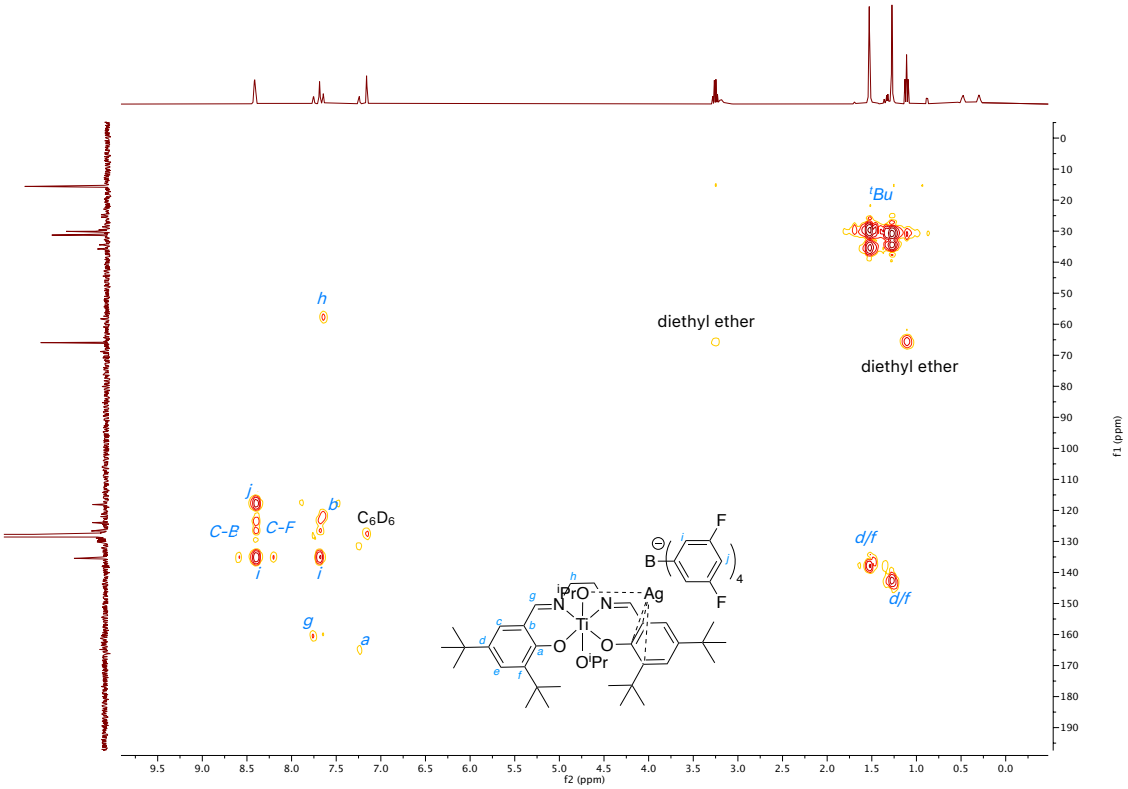

Figure S8: HMBC NMR spectrum of **1-AgBArF** *in-situ* generated by addition of equimolar AgBArF to **1** in C_6D_6.

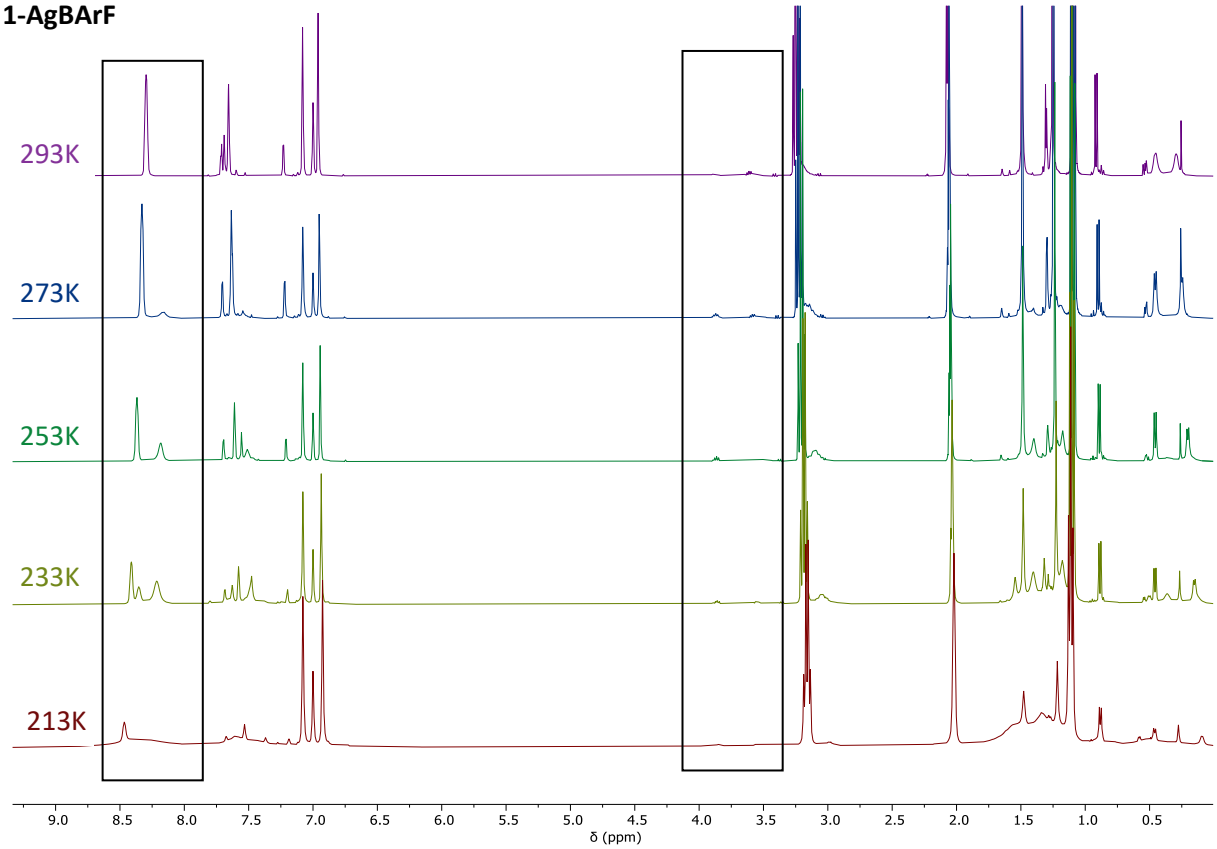

Figure S9: ^{1}H NMR spectra (toluene-d_8)of **1-AgBArF** at variable temperature (213 K < T < 293 K), selected area shown in Figure S10 and Figure S11.

^{1}H NMR spectra (toluene-d_8) of **1-AgBArF** at variable temperatures (233 K < T< 293 K) show multiple species proposed to be in equilibrium at room temperature as deduced from the characteristic signals of the BArF counter-anions (8.70 ppm < δ < 8.00 ppm, Figure S10) and the OiPr groups (3.30 ppm < δ < 4.25 ppm, Figure S11). Among the signals of interest, the signals related to the protons in ortho positions of BArF moiety shows that the counter-anion is experiencing at least three different environments at 233K (Figure S10). Similarly, the signals attributed to the isopropyl proton [i.e. CH-$(CH_3)_2$] of one of the O^{i}Pr group show broad resonances and at least two different environments (Figure S11). The different species are proposed to be different isomers of **1-Ag^{+}** as described in Figure S27-S28.

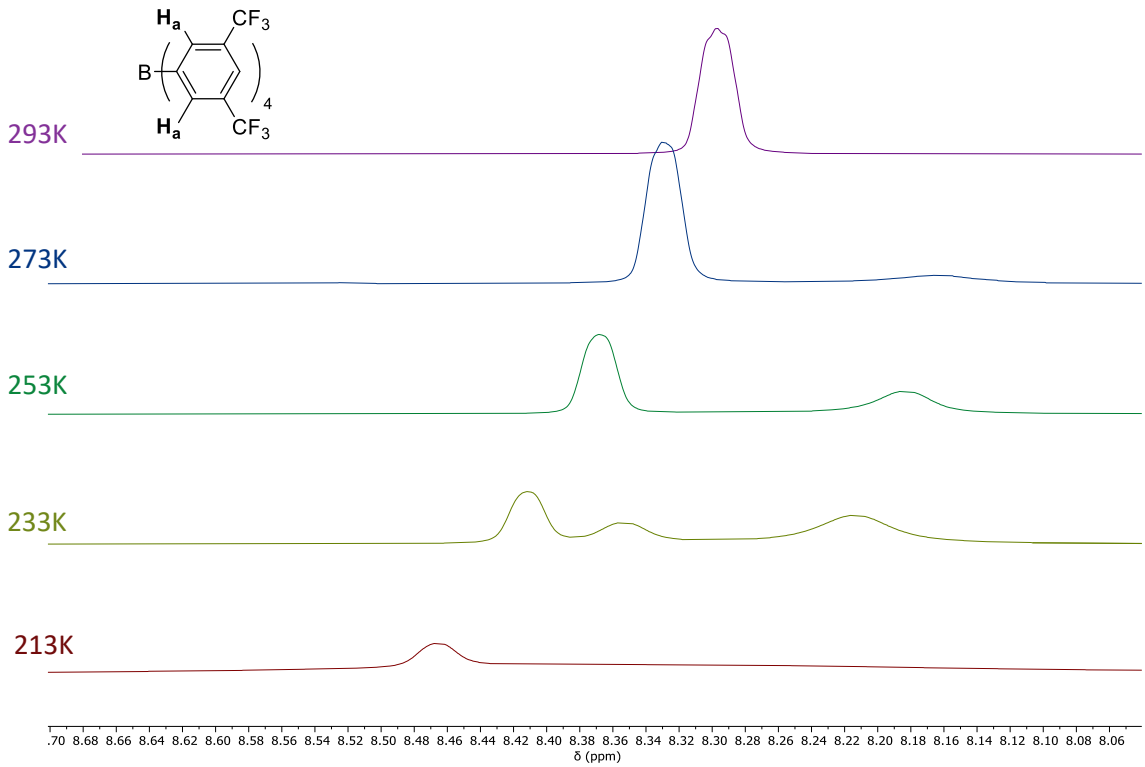

Figure S10:[1]H NMR spectra (toluene-d_8, 8.06 ppm < δ < 8.70 ppm) of **1-AgBArF** showing different environments for the BArF counter-anions (signals attributed to H_a) at variable temperature (213 K < 293 K) and suggesting multiple species in equilibrium.

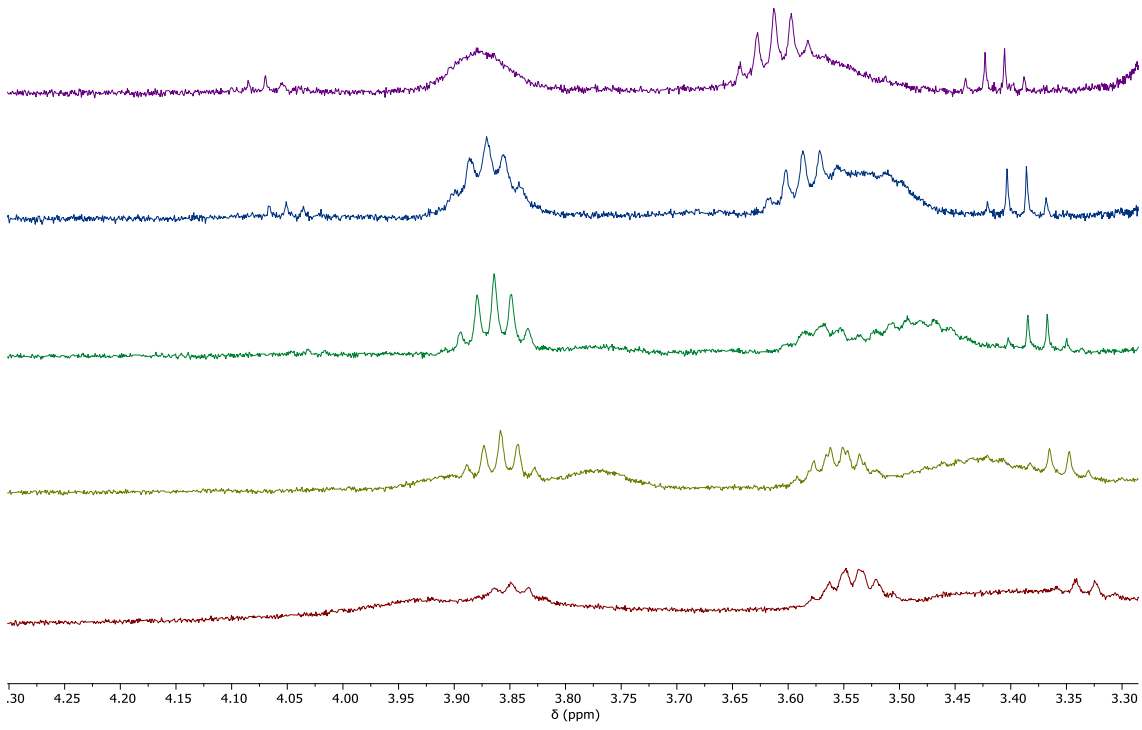

Figure 11: [1]H NMR spectra (toluene-d_8, 8.06 ppm < δ < 8.70 ppm) of **1-AgBArF** showing different environments for the O^{i}Pr groups (O-C*H*-(Me)$_2$) at variable temperature (213 K < 293 K) and suggesting multiple species in equilibrium.

Polymerisation data:

Table S1: Data for rac-LA ROP initiated by **1** at 90°C toluene.

Entry	Time (h)	Conversion[a] (%)	$M_{n(calc.)}$[b] (kg mol^{-1})	$M_{n(exp.)}$[c] (kg mol^{-1})	Đ[c]
1	1	12	1.7	1.2	1.54
2	2	24	3.5	1.9	1.62
3	4	44	6.3	4.0	1.28
4	10	54	7.8	5.0	1.41
5	24	73	10.5	6.6	1.29

*Reaction conditions: **1**/AgOTf/rac-LA = 1:1:100 with $[rac\text{-}LA]_0$ = 1 M in toluene, **1** and AgOTf = 5 mmol (1 equiv.) reaction at 90°C.[a]Determined from the relative integrals in the ^{1}H NMR (PLA = 5.30 – 5.10 ppm and LA = 5.07 – 4.96 ppm). [b]Calculated using formula $M_{n(calc.)}$ = conv. (%)*144.13(g mol^{-1}). [c]GPC analysis in THF with flow rate 1 mL min^{-1} calibrated using narrow-M_n polystyrene standards and $M_{n(exp)}$ corrected by factor 0.58.*[7]

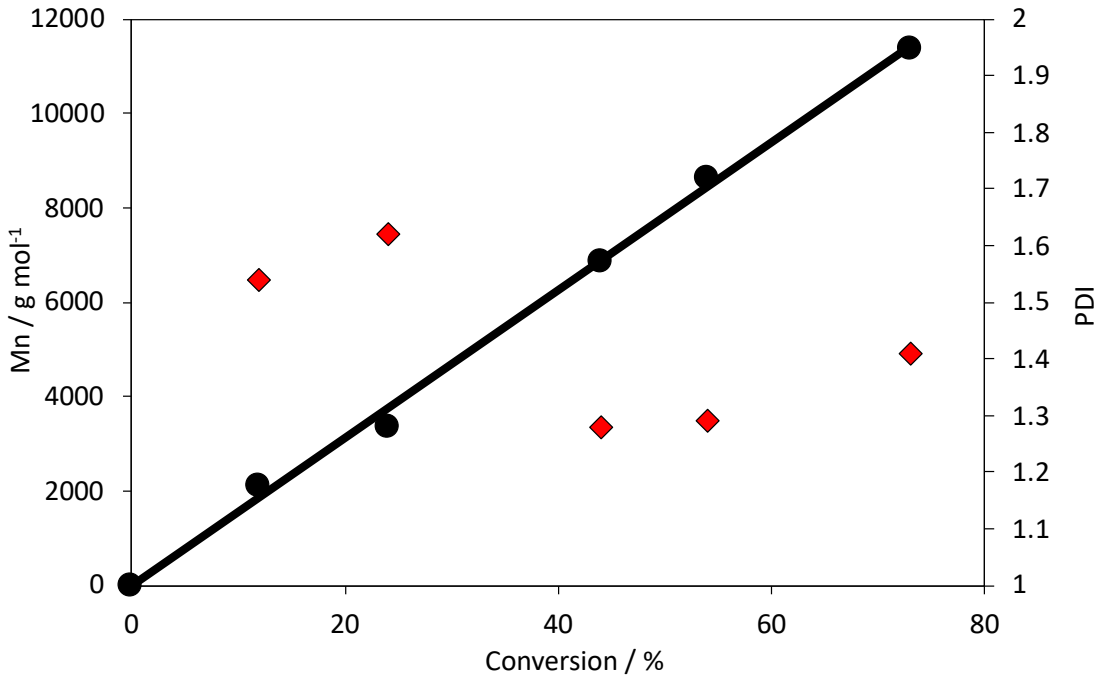

Figure S12: **1**/rac-LA = 1:100 with $[rac\text{-}LA]_0$ = 1 M in toluene and, **1** = 5 mmol reaction at 363 K. Black - plot of number-average molecular weight (Mn) vs conversion (%). Red - plot of the PDI values vs. conversion.

Table S2: Data for rac-LA ROP initiated by **1** + AgBArF at room temperature in DCM.

Entry	**Time** (min)	**Conversion**[a] (%)	$M_{n(calc.)}$[b] (kg mol^{-1})	$M_{n(exp.)}$[c] (kg mol^{-1})	**Đ**[c]
1	10	24	3.4	1.8	1.5
2	20	38	5.5	4.9	1.3
3	30	53	7.6	6.8	1.3
4	40	59	8.5	8.0	1.2
5	50	70	10.2	8.2	1.2
6	60	76	10.9	9.5	1.2
7	70	83	12.0	10.3	1.2

*Reaction conditions: **1**/AgBArF/rac-LA = 1:1:100 with $[rac\text{-}LA]_0$ = 1 M in DCM, **1** and AgOTf = 5 mmol (1 equiv.) reaction at 90°C. [a]Determined from the relative integrals in the ^{1}H NMR (PLA = 5.30 – 5.10 ppm and LA = 5.07 – 4.96 ppm). [b]Calculated using formula $M_{n(calc.)}$ = conv. (%)*144.13(g mol^{-1}). [c]GPC analysis in THF with flow rate 1 mL min^{-1} calibrated using narrow-M_n polystyrene standards and $M_{n(exp)}$ corrected by factor 0.58.*[7]

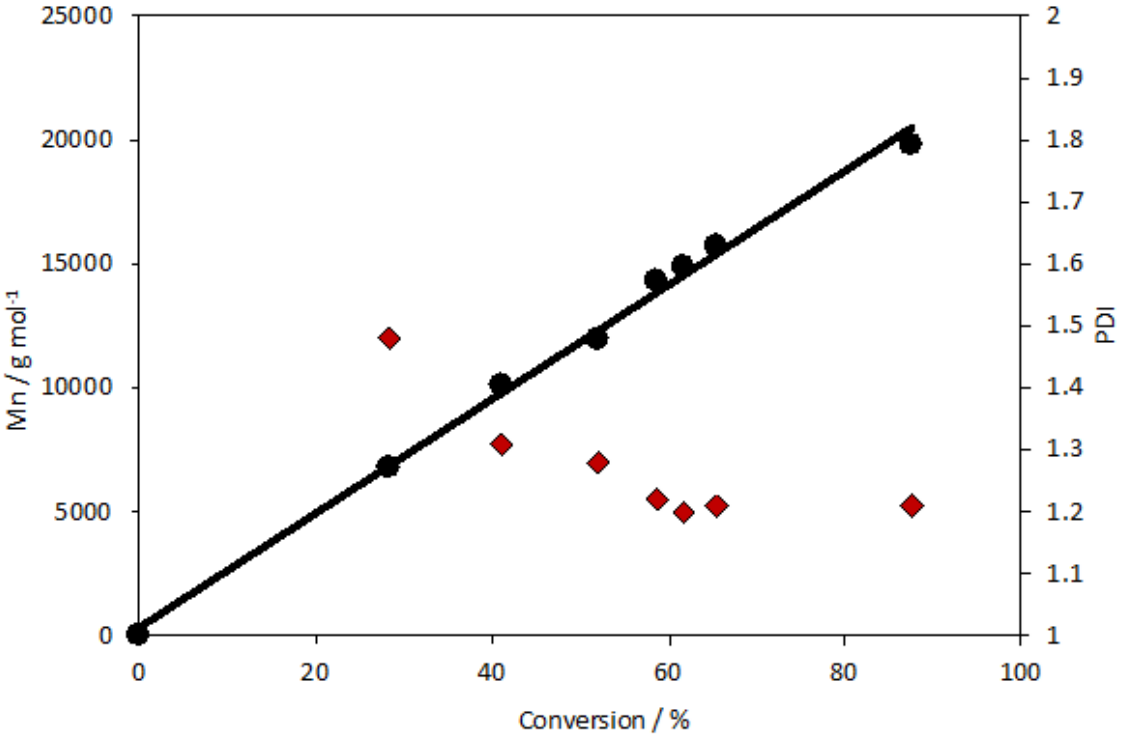

Figure S13: **1**/AgBArF/rac-LA = 1:1:100 with $[rac\text{-}LA]_0$ = 1 M in DCM, **1** and AgBArF = 5 mmol reaction at 298 K. Black - plot of number-average molecular weight (Mn) vs conversion (%). Red - plot of the PDI values vs. conversion.

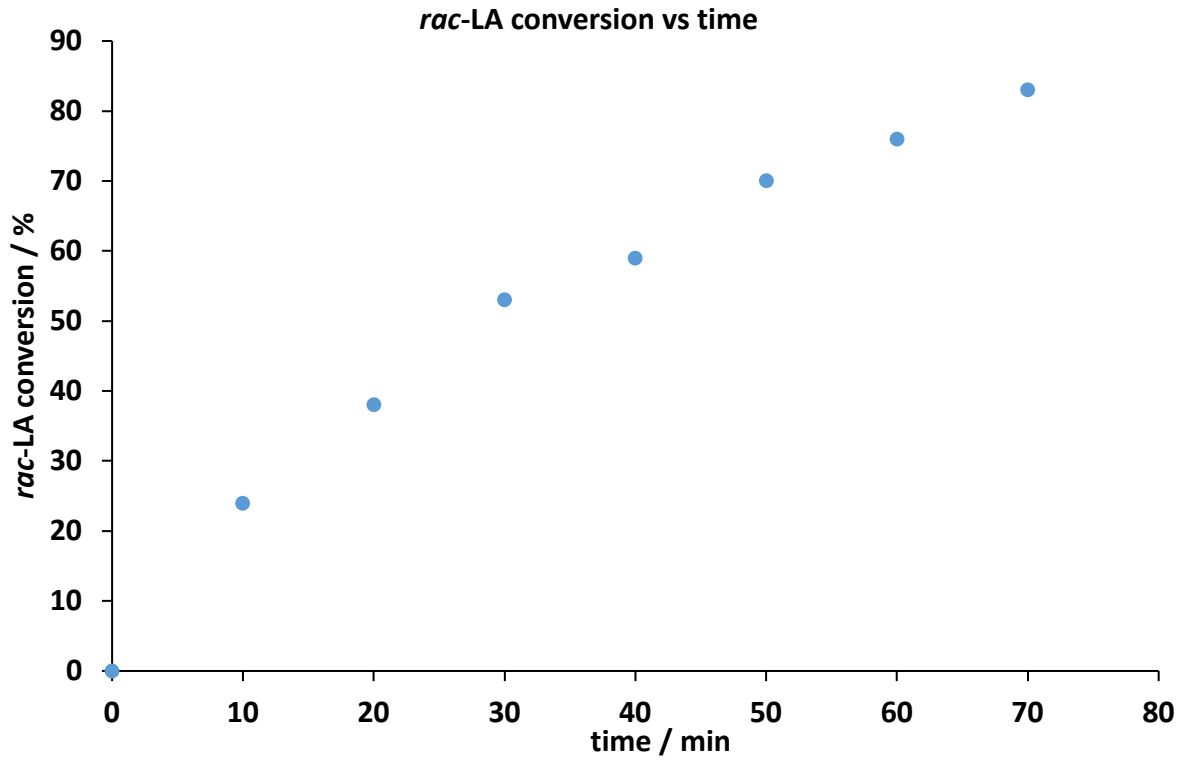

Figure S14: *rac*-LA conversion (%) versus time (min) for *rac*-LA ROP initiated by **1-AgBArF** as per Table S2.

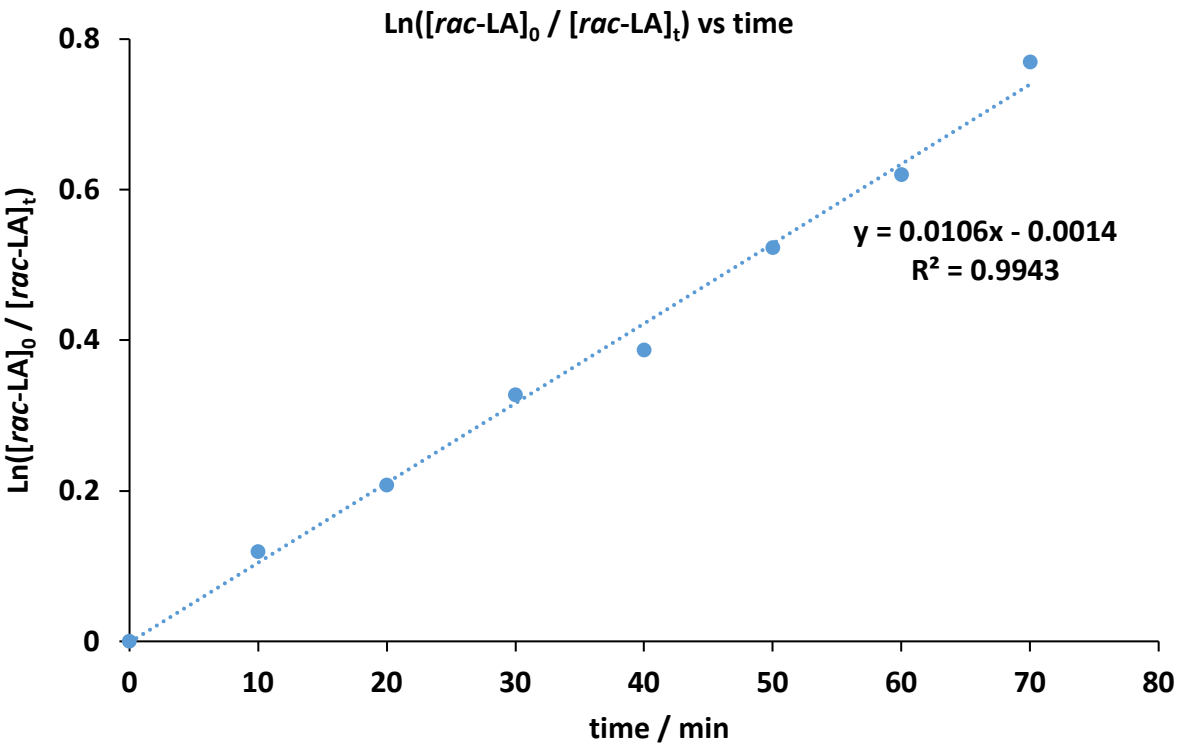

Figure S15: Ln([*rac*-LA]$_0$ / [*rac*-LA]$_t$) vs time (min) for *rac*-LA ROP initiated by **1-AgBArF** as per Table S2.

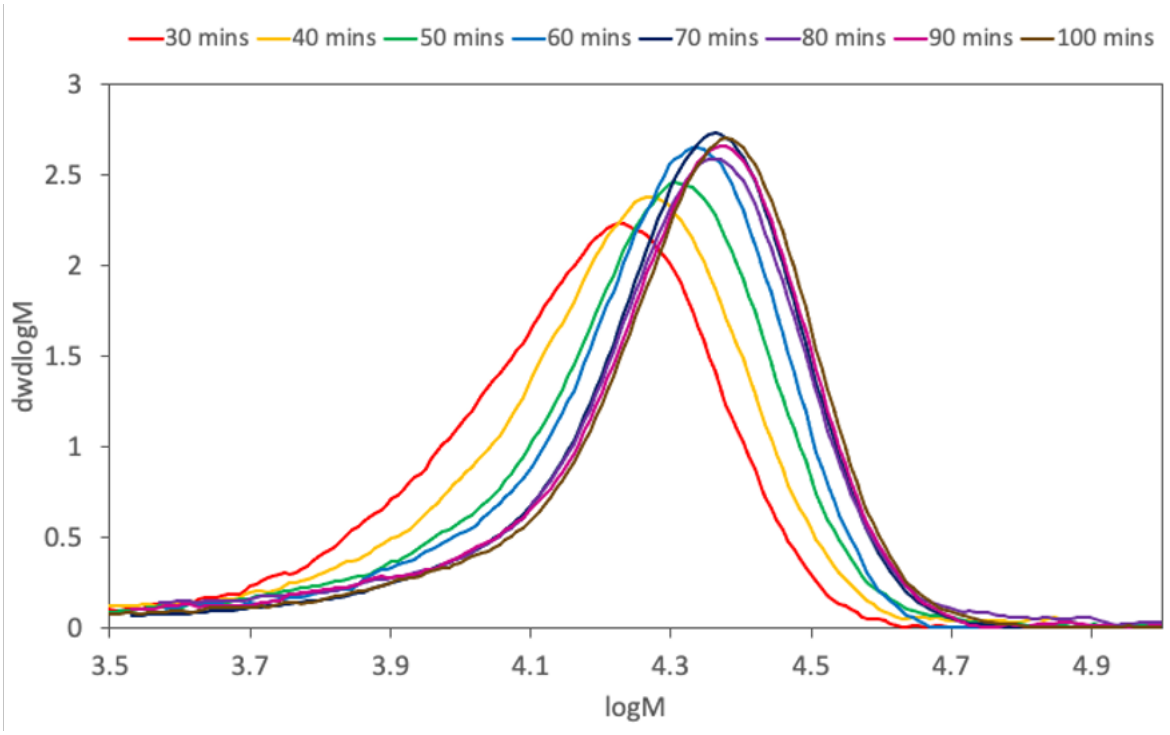

Figure S16: Overlay of molar mass distribution as per data in Table S2 from GPC analysis.

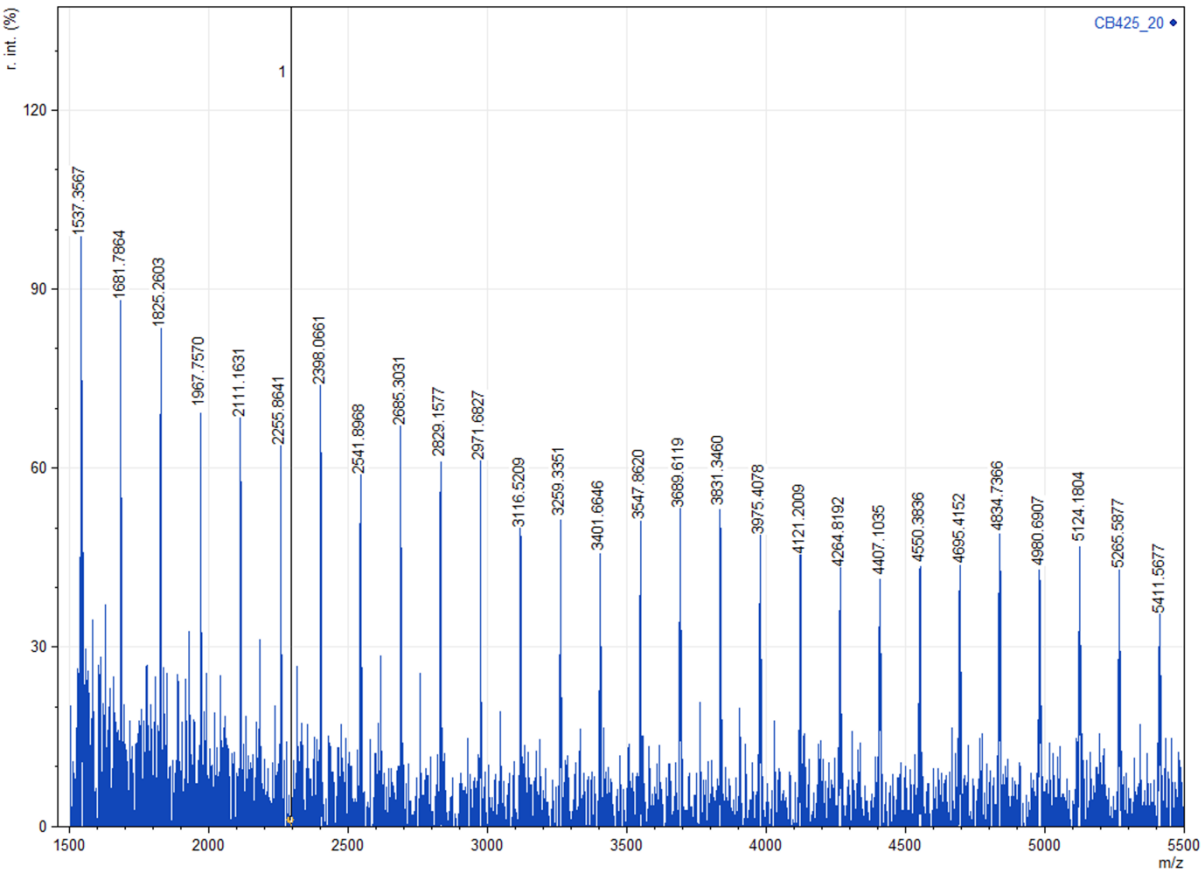

Figure S17: MALDI-ToF spectrum of PLA (1500 < m/z < 5500) showing peaks spaced by 144 (conditions as per Entry 2, Table S2, data available at DOI: 10.14469/hpc/8762).

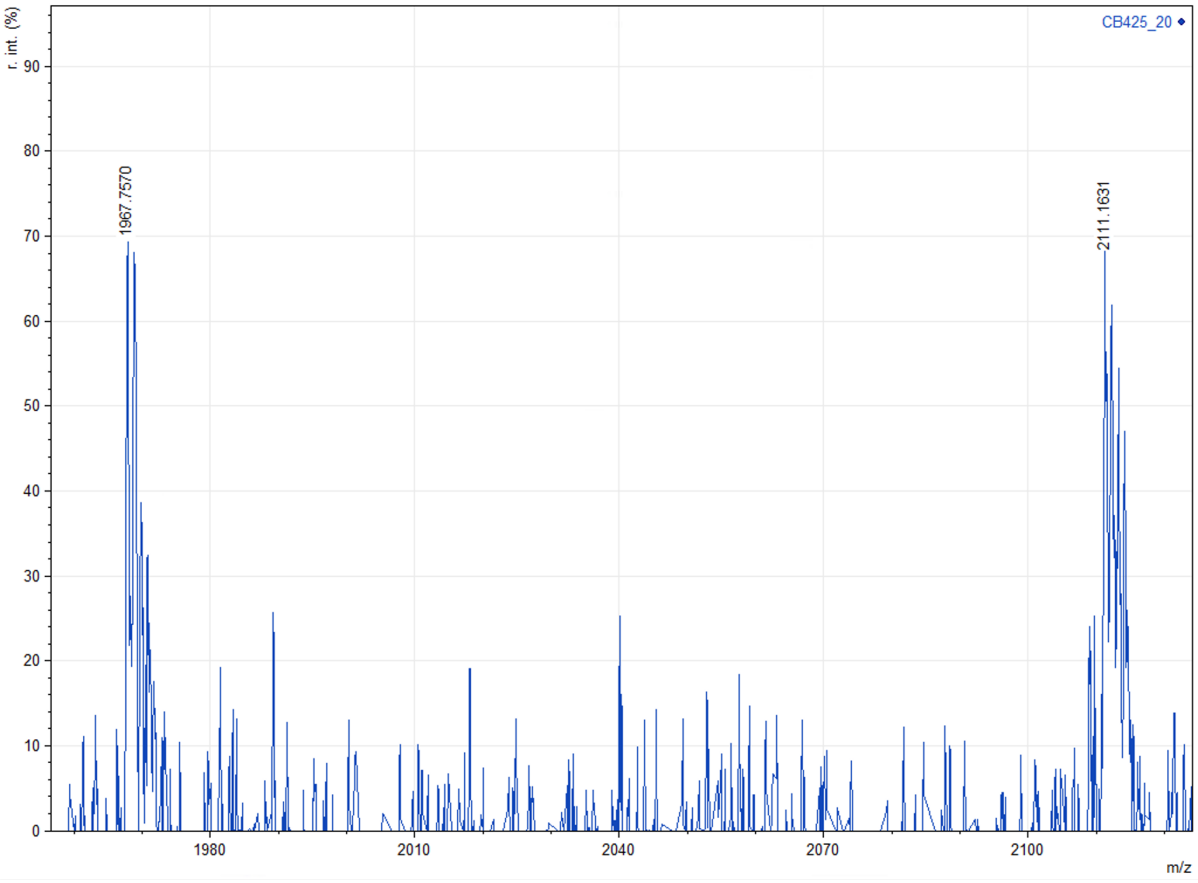

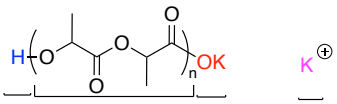

$M_{n(K)}$ = 1.0078 + n x 144.0423 + 54.9586 + 38.9637

n	$M_{n(K)}$	$M_{n(exp)}$	$\lvert\Delta M_n\rvert$
13	1967.5800	1967.7570	0.17
14	2111.5223	2111.1631	0.36

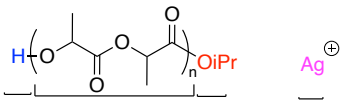

$M_{n(Ag)}$ = 1.0078 + n x 144.0423 + 54.9586 + 109.9051

n	$M_{n(Ag)}$	$M_{n(exp)}$	$\lvert\Delta M_n\rvert$
12.5	1967.4914	1967.7570	0.27
13.5	2111.5337	2111.1631	0.37

Figure S18: MALDI-ToF spectrum (zoom) of PLA suggesting formation of linear polymers (as per Table S2, Entry 2, data available at DOI: 10.14469/hpc/8762).

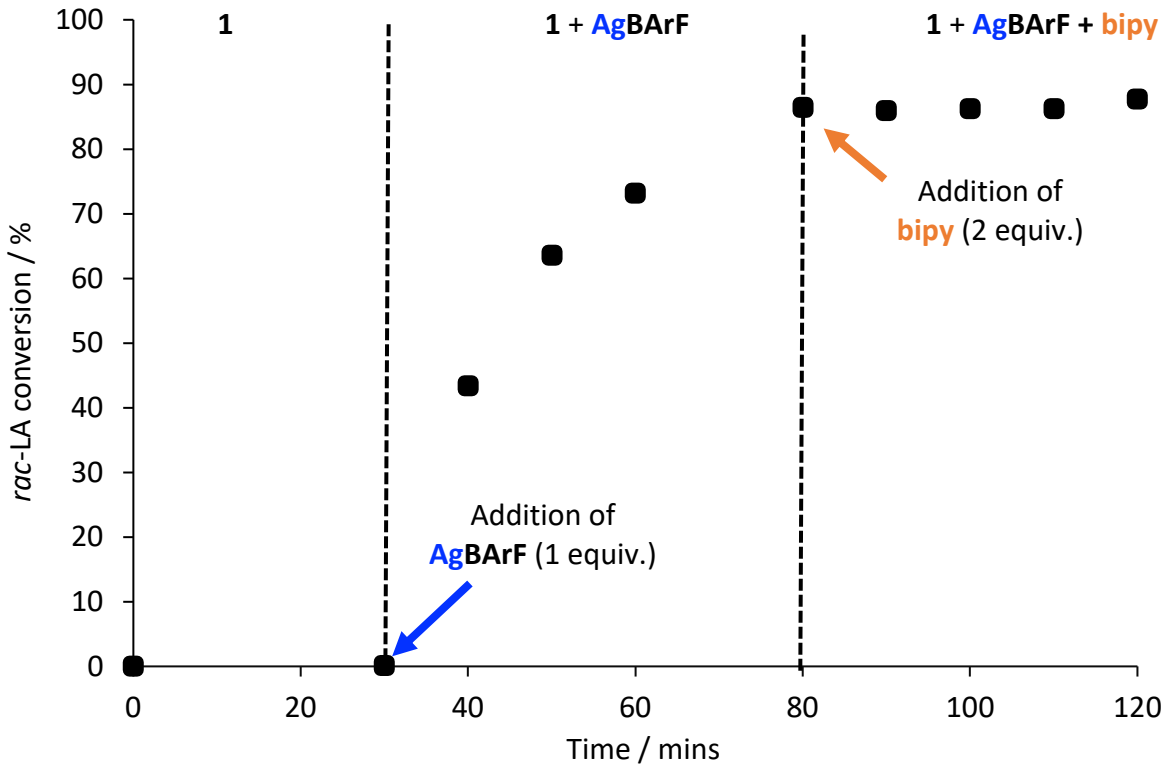

Figure S19: Plot of *rac*-LA conversion vs. time showing i) addition of **AgBArF** to **1**/*rac*-LA (1:100) after 30 min triggers *rac*-LA ROP, and ii) addition of **bipy** after 80 min stops *rac*-LA ROP.

Reactivity Study

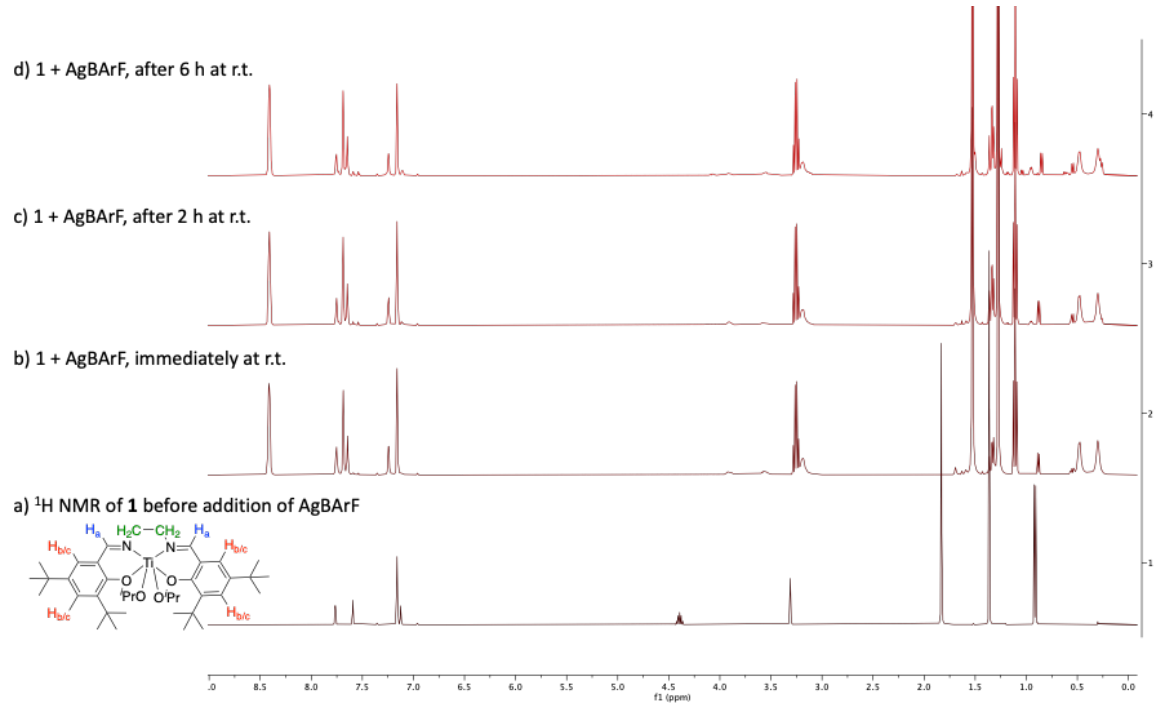

Figure S20: ^{1}H NMR spectrum overlay (400 MHz, C_6D_6, full spectrum) of the reaction **1** + AgBArF (1:1) in C_6D_6 showing the formation of stable **1-AgBArF** up to 6 hours at room temperature (signal integrations for spectra a) and b) as per Figure S1 and Figure S5, respectively, data available at DOI: 10.14469/hpc/9854).

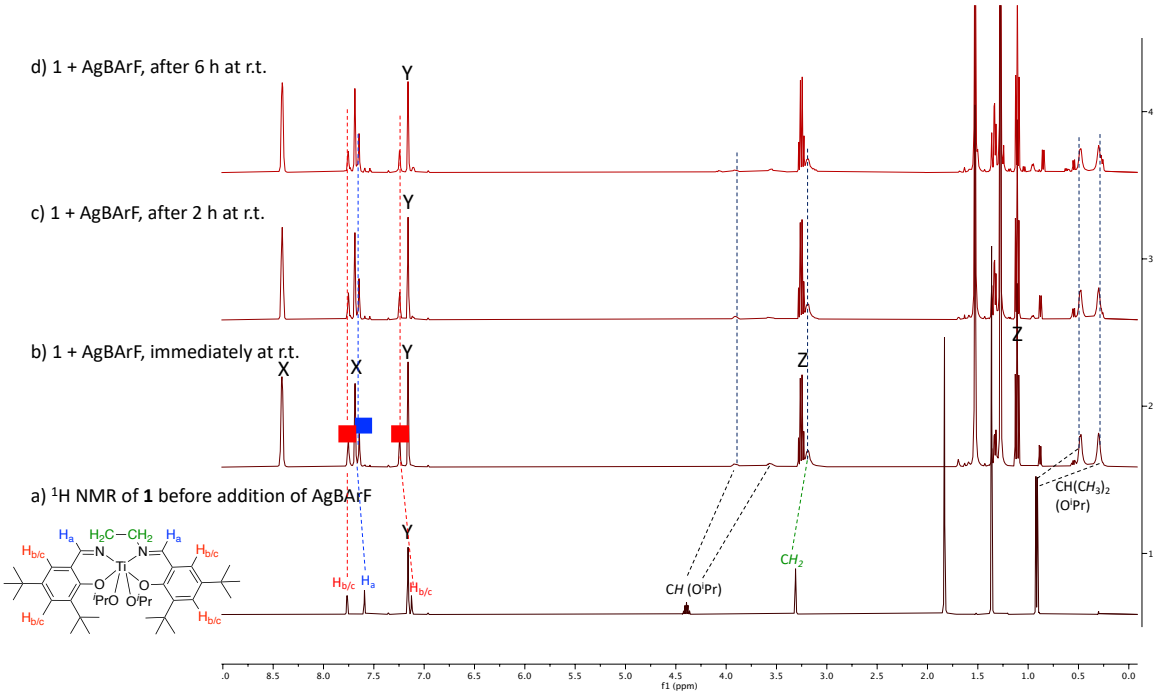

Figure S21: ^{1}H NMR spectrum overlay (400 MHz, C_6D_6, in the range 3.00 - 8.50 ppm (zoom from Figure S8) of the reaction **1** + AgBArF (1:1) in C_6D_6 showing the formation of **1-AgBArF** (signal integrations for spectra a) and b) as per Figure S1 and Figure S5, respectively, data available at DOI: 10.14469/hpc/9854)

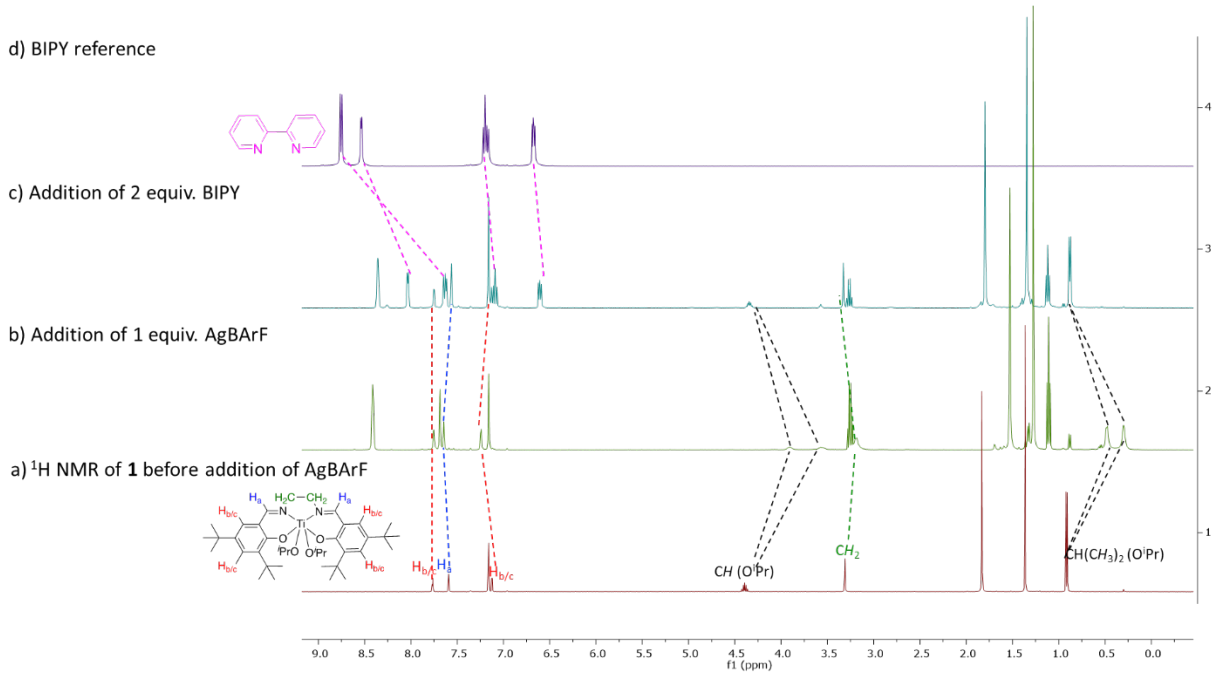

Figure S22 ^{1}H NMR spectrum overlay (400 MHz, C_6D_6) indicating the changes when 1 equiv. AgBArF is added to **1** and then 2 equiv. bipy are added, reforming **1** alongside a hypothesised $(bipy)_2AgBArF$ complex.

DOSY NMR experiments

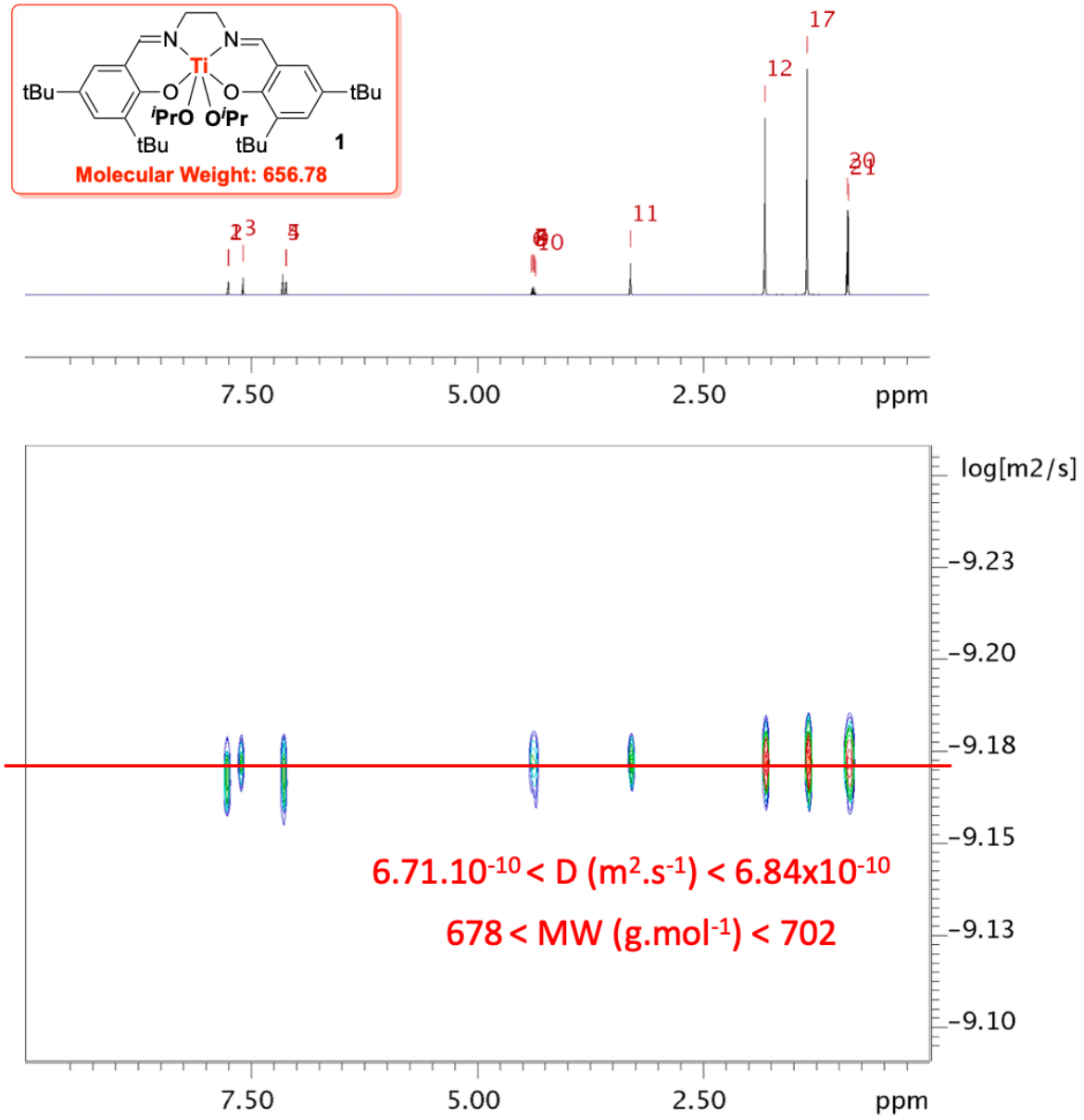

Figure S23: DOSY (500 MHz, C_6D_6) NMR spectrum of **1** suggesting a monomeric species in solution (molecular weight estimated using *in-house* calibration curve).

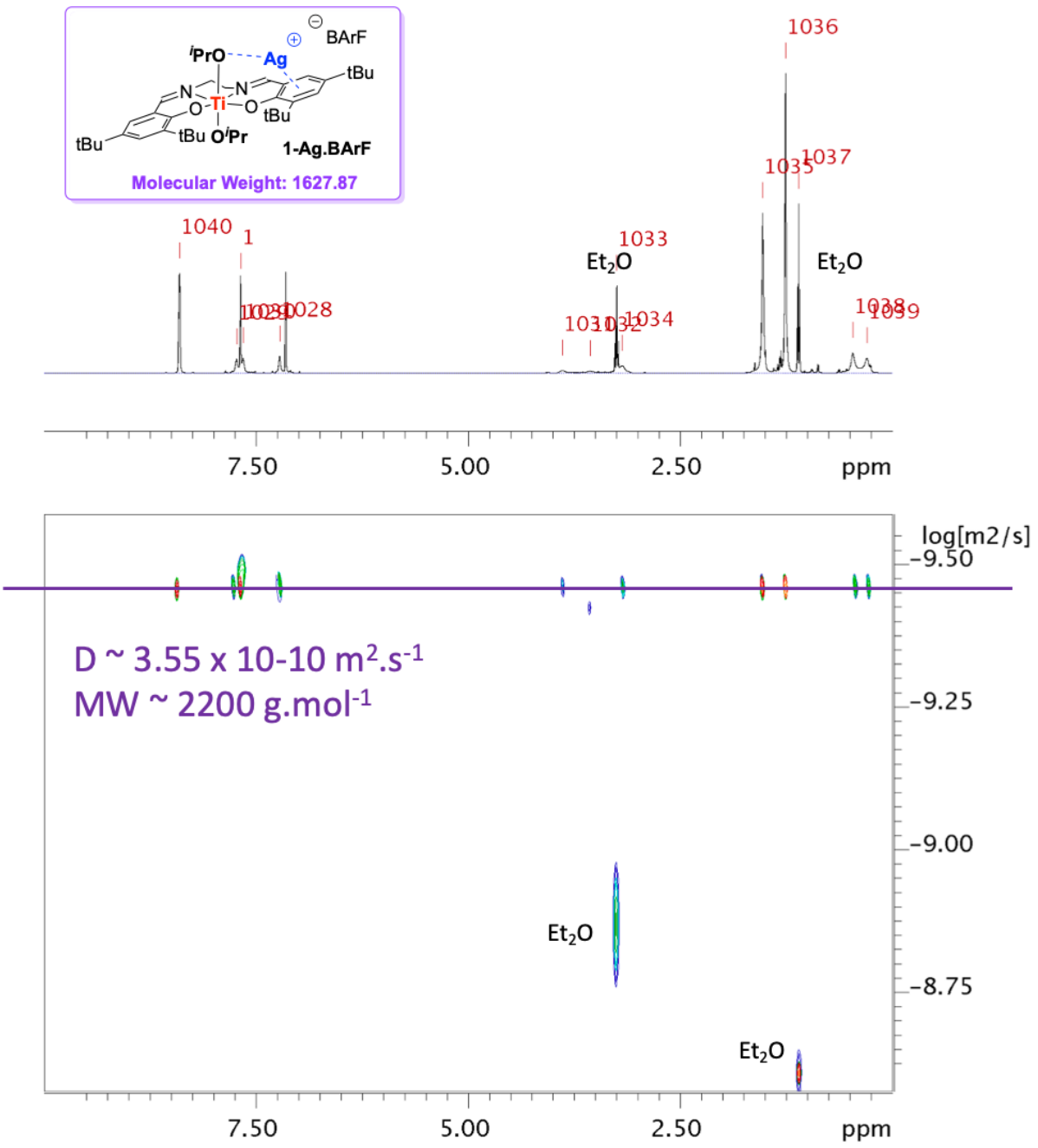

Figure S24:DOSY NMR spectrum of **1-AgBArF** (*in-situ* generated by equimolar addition **1** + **AgBArF**) showing formation of a single aggregated species.

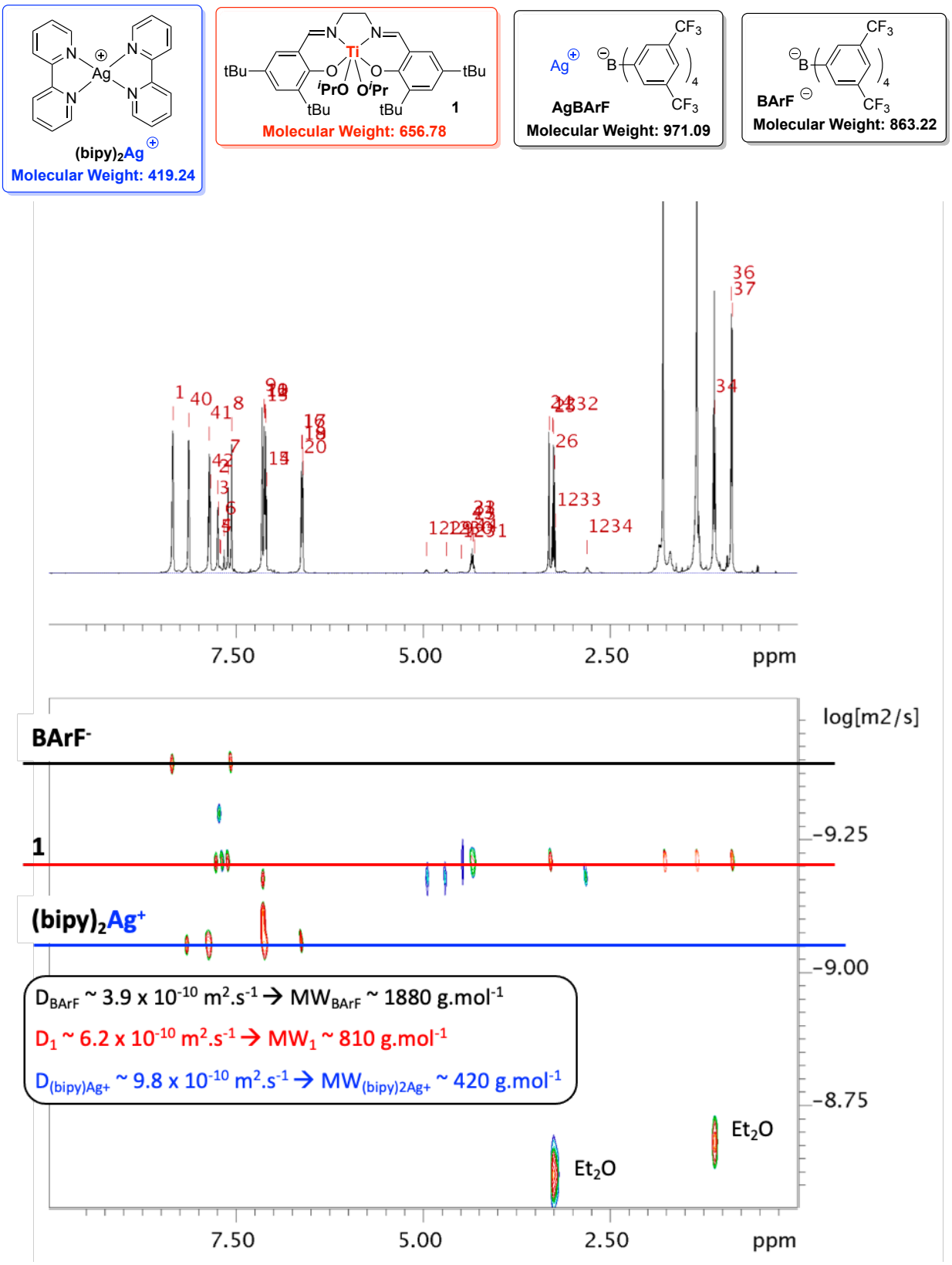

Figure S25: DOSY NMR spectrum (C_6D_6, 500 MHz) in line with the formation of **1** and cationic complex **(bipy)$_2$Ag$^+$** upon addition of 2 equiv. of bipy to **1-AgBArF** (*in-situ* generated).

UV-Vis Spectroscopy

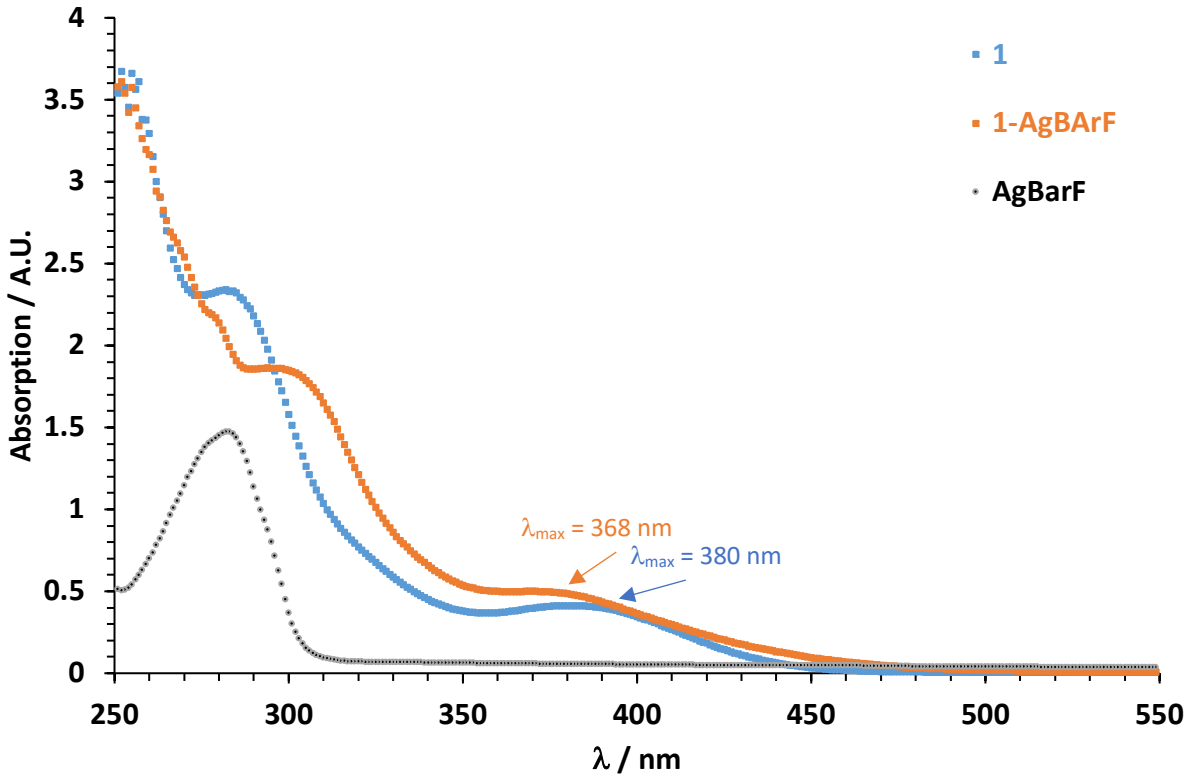

Figure S26: UV-vis absorption spectra of **1** (blue), **1- AgBArF** (*in-situ* generated, orange) and **AgBArF** (grey) in DCM (c = 100 μM), data available at DOI: 10.14469/hpc/8763.

Computational details

General considerations: DFT calculations were performed using Gaussian 16 (revision C01).[8] Unless stated otherwise, calculations were performed at 298.15K (default) and used the ωB97xD density functional (which includes a second-generation dispersion and long-range corrections) with Def2-SVP basis set (from the Basis Set Exchange).[9] Unless stated otherwise, self-consistent reaction cavity continuum solvation model was used with benzene as the solvent [scrf=(cpcm, solvent=benzene)]. All transition states were characterized by normal coordinate analysis revealing precisely one imaginary mode corresponding to the intended reaction. For **V-Ag$^+$-TS** and **VII'-Ag$^+$-TS** IRC calculations were performed which also confirmed the identity of the transition states. Full coordinates for all the stationary points are available at DOI: 10.14469/hpc/8729.

Optimised geometry pictures were generated from Gaussian files using CYLView 2.0 available at http://www.cylview.org.[10]

NCI surfaces were created using JMol 13.2.8 and cub files (SCF total density, grid: fine) generated from GaussView 6.1.1. The following parameters were used to create the NCI surface (a low cut-off of 0.02 was used to remove the covalent density surrounding the Ti and Ag atoms and a relatively large surface cut-off of 0.8 was used):

```
isosurface parameters [0.8, 1.0, 0.0002, 0.02, 0.95, 1.0] NCI "";
      colorscheme "bgyor";color isosurface range 0.04 -0.04
```

Electrostatic Potential Surfaces were generated using Multiwfn3.8 and the associated scripts.[11]

GoodVibes 3.0.2 has been used to calculate Gibbs free energies (ΔG_{298}) in Table S4 to take into consideration the deviation that could be due to low frequencies.[12]

Natural Bond Orbital (NBO) analysis were carried out using the NBO 6 program.[13]

Natural orbitals and molecular orbitals were plotted using Gaussview 6.1.1.

Methods: For computational efficiency, the O^{i}Pr groups of **1** were replaced by OMe (referred to as **I**) and the weakly coordinating counter-anion BArF was omitted.[14] The molecular structure for the *trans* configuration of **I** was deduced from the molecular structure (deduced from X-Ray diffraction) of a dichloro titanium salen complex bearing the same ligand.[15] The molecular structure for the *cis*-beta configuration of **I** was deduced form the molecular structure (deduced from X-Ray) of a dimeric titanium salen complex bearing the same ligand.[16]

Attempts to coordinate an Ag$^+$ atom to the oxygen atoms of the phenolate moieties (i.e. k^2 coordination) as previously observed for unsubstituted Cu salen complexes was unsuccessful due to the bulkiness of the ^{t}Bu groups.[17] Instead, the Ag$^+$ atom was found to coordinate with the phenolate moiety via cationic-Π interactions as well as with one of the oxygen atom of one of the methoxy groups forming complex **I-Ag$^+$**. The calculated Ag – C_{arene} distances (e.g. d(Ag - C_{ipso}) = 2.64 Å, d(Ag-C_{ortho}) = 2.87 Å) where found below 3.90 Å (value usually considered to establish hapticity, the sum of the van der Waals radii of silver and carbon being 3.80 Å).[18] The calculated Ag-C_{arene} distances lie within the range of distances experimentally observed for structurally characterized Ag$^+$-arene complexes,[14] and metal salen complexes coordinating Ag$^+$ atoms in a similar fashion [e.g. 2.47 Å < d(Ag-C_{arene}) < 2.70 Å].[17c, 19] In addition, the electrostatic potential surface of **I** supports such a coordination of an Ag$^+$ atom above and shifted away from the phenolate ring centroid (i.e. short Ag-C_{ipso} distance), in agreement with previous theoretical studies for cation-Π interactions of phenol and catechol with mono cations.[20] The resulting coordination of Ag$^+$ leads to elongated and shortened Ti-O(Me) bonds in **I-Ag$^+$**, compared to distances observed in **I**.

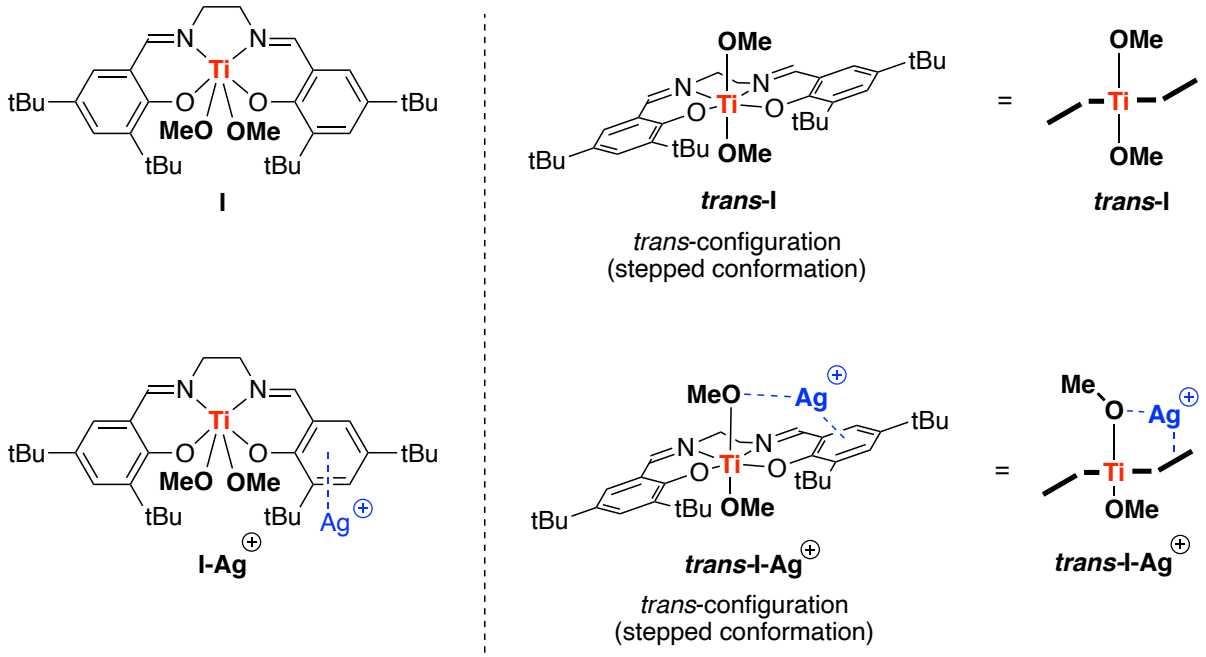

Figure S27: Different interactions of **I** in trans configuration (***trans*-I**) with Ag^+ (data available at DOI: 10.14469/hpc/8749).

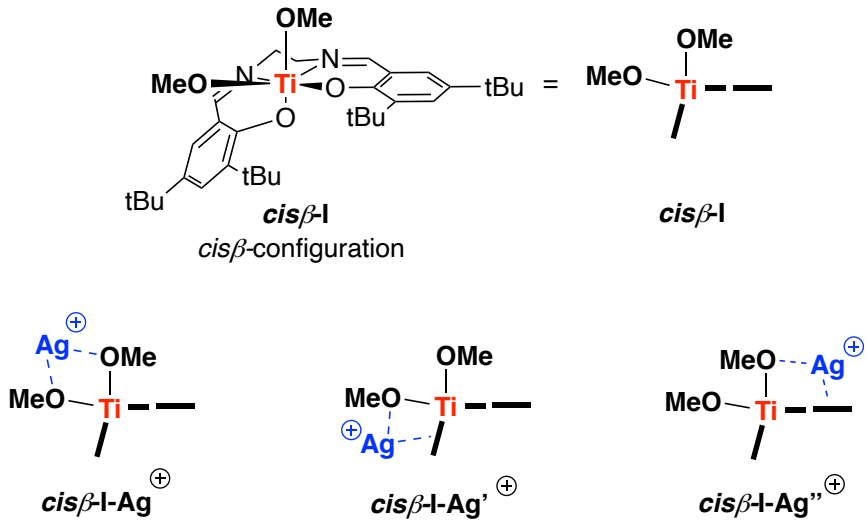

Figure S28:Different interactions of **I** in a cis-β configuration (**cisβ-I**) with Ag^+ (data available at DOI: 10.14469/hpc/8749).

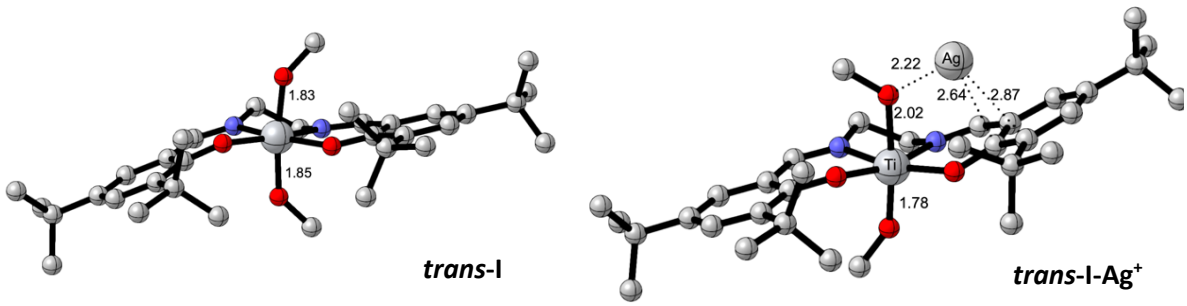

Figure S29: Optimised geometries (H atoms omitted) of **trans-I** and **trans-I-Ag$^+$** (ωB97xD/Def2-SVP, cpcm=benzene) showing binding of Ag$^+$ and elongation of one Ti-$O_{(OMe)}$ bond (data available at DOI: 10.14469/hpc/8749)

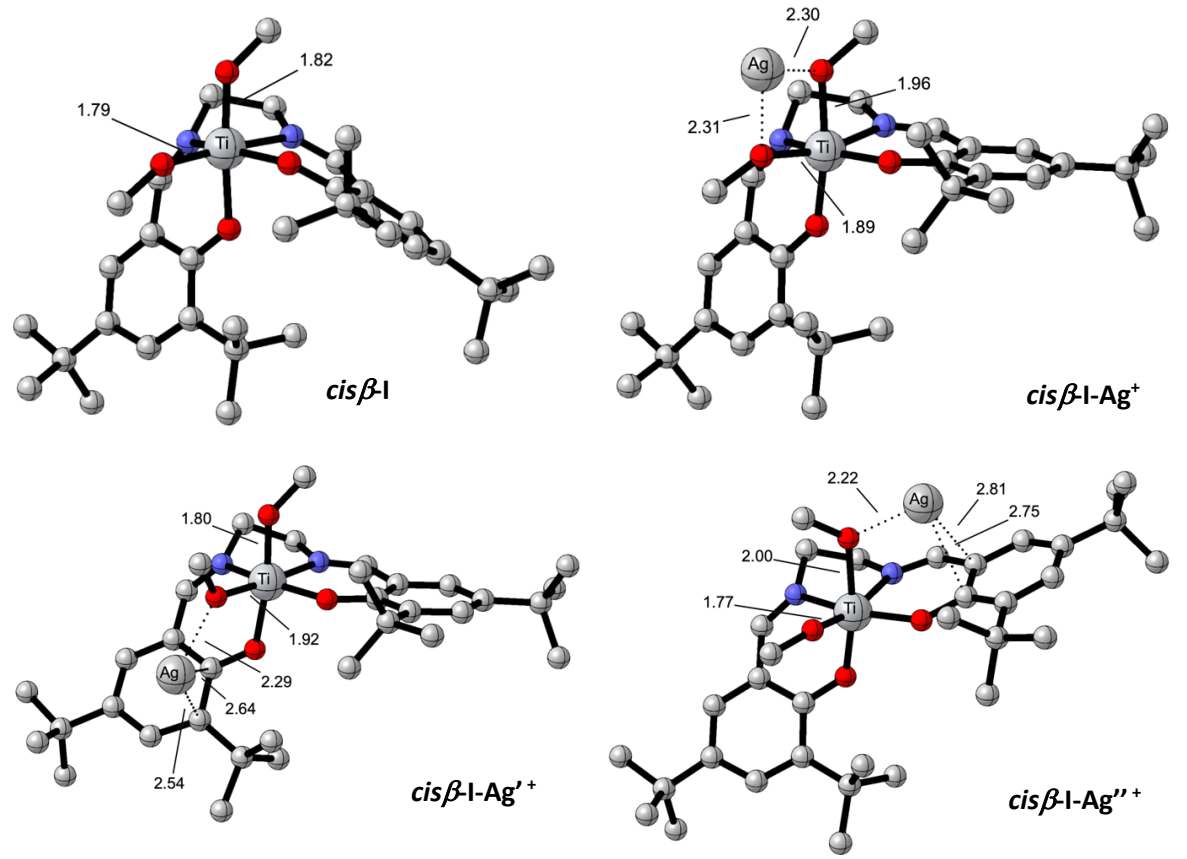

Figure S30: Optimised geometries (H atoms omitted) of **I** in cisβ-configuration and binding with Ag$^+$ (ωB97xD/def2-svp, cpcm = benzene, data available at DOI: 10.14469/hpc/8749).

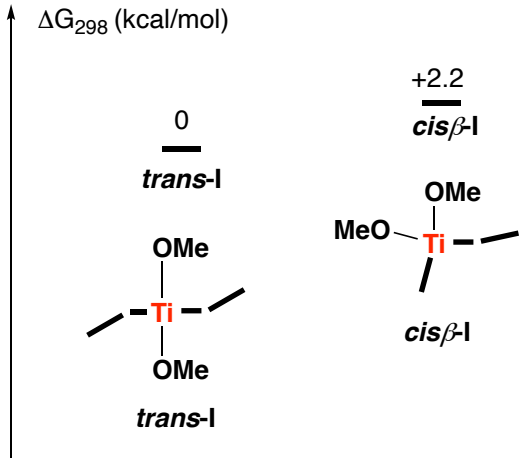

Figure S31: Relative Gibbs free energies of ***trans*-I** and ***cis*β-I** showing the *trans* configuration being the most stable (data available at DOI: 10.14469/hpc/8749)

As a mononuclear species in solution (in line with the DOSY experiments, see Figure S20), **I** preferably adopts a *trans*-configuration (referred to as ***trans*-I**) along with a *mer*-coordination of the salen ligand (Figure S28), as generally observed for other Ti(IV) salen complexes,[21] including dialkoxide derivatives,[22] dihalogenato derivatives, [15, 23] dialkyl aderivatives[24] and oxo derivatives.[25]

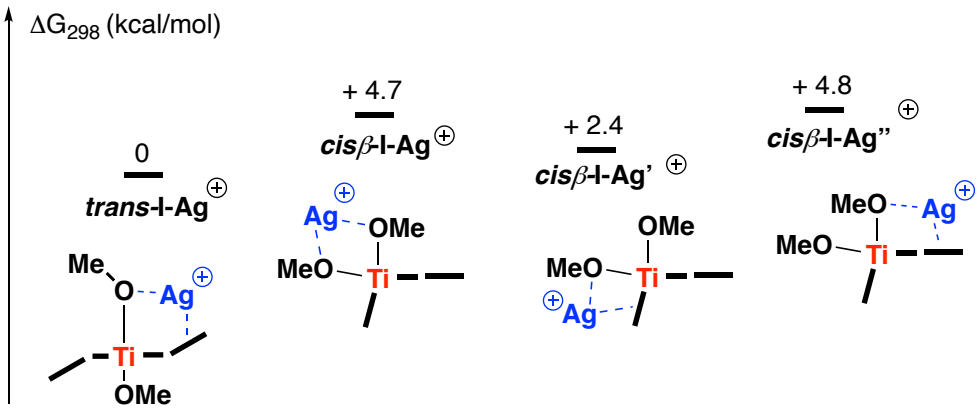

Figure S32: Relative Gibbs free energies (ΔG_{298}) of heterobimetallic Ti-Ag species **I-Ag$^+$** for trans- and cisβ-configurations showing the trans configuration ***trans*-I-Ag$^+$** being the most favourable (data available at DOI: 10.14469/hpc/8749).

Table S3: Relative Gibbs free energies (ΔG_{298}) for **I** and **I-Ag$^+$** using ωB97xD/Def2-SVP and M06-2X/Def2-SVP showing the *trans* configurations being the most favoured (data available at DOI: 10.14469/hpc/8749)

	ωB97xD/Def2-SVP			**M06-2X/Def2-SVP**		
	ΔG_{298} (Hartree)	ΔG_{298} (kcal/mol)	DOI:	ΔG (Hartree)	ΔG (kcal/mol)	DOI:
***trans*-I**	-2584.472732	0 (ref)	10.14469/hpc/8750	-2584.122713	0 (ref)	10.14469/hpc/8756
***cisβ*-I**	-2584.469182	+2.23	10.14469/hpc/8751	-2584.11909	+2.3	10.14469/hpc/8757
***trans*-I-Ag$^+$**	-2731.338962	0 (ref)	10.14469/hpc/8752	-2730.881513	0 (ref)	10.14469/hpc/8758
***cisβ*-I-Ag$^+$**	-2731.331514	+4.7	10.14469/hpc/8753	-2730.873595	+5.0	10.14469/hpc/8759
***cisβ*-I-Ag'$^+$**	-2731.331304	+2.4	10.14469/hpc/8754	-2730.87914	+1.5	10.14469/hpc/8760
***cisβ*-I-Ag''$^+$**	-2731.33518	+4.8	10.14469/hpc/8755	-2730.874385	+4.5	10.14469/hpc/8761

Table S4: Relative Gibbs free energies (ΔG_{298}) for **I** and **I-Ag$^+$** calculated using Gaussian (rigid-rotor harmonic oscillator RRHO treatment) and GoodVibes (quasi-harmonic oscillator treatment, using Grimme or Truhlar treatment) at ωB97xd/Def2-SVP, cpcm=benzene level.

	Gaussian 16 (C01)	GoodVibes[a]	
		Grimme[b]	Truhlar[c]
***trans*-I**	0 (ref)	0 (ref)	0 (ref)
***cisβ*-I**	+2.23	+1.86	+ 1.50
***trans*-I-Ag$^+$**	0 (ref)	0 (ref)	0 (ref)
***cisβ*-I-Ag$^+$**	+4.67	+4.65	+4.93
***cisβ*-I-Ag'$^+$**	+2.37	+2.75	+2.90
***cisβ*-I-Ag''$^+$**	+4.81	+4.97	+5.08

a) Using GoodVibes with a frequency cut-off value of 100 wavenumbers; b) Grimme treatment using a mixture of RRHO (above cut-off value) and free rotor vibrational entropies (below cut-off value) along with a damping function close to the cut-off value; c) Using Truhlar treatment where low frequencies are adjusted to the cut-off value (i.e. 100).

```
python3 -m goodvibes salen/*.log -f 100 -qs truhlar
```

```
Entropic quasi-harmonic treatment: frequency cut-off value of 100.0 wavenumbers will be applied.
QS = Truhlar: Using an RRHO treatment where low frequencies are adjusted to the cut-off value.
REF: Ribeiro, R. F.; Marenich, A. V.; Cramer, C. J.; Truhlar, D. G. J. Phys. Chem. B 2011, 115, 14556-14562

Structure                                    E        ZPE            H        T.S     T.qh-S          G(T)       qh-G(T)
*************************************************************************************************************************
I-Ag                                 -2732.070316   0.811234  -2731.210792   0.128169   0.117268  -2731.338961  -2731.328059
I-cisB                               -2585.203482   0.809879  -2584.347323   0.121859   0.113256  -2584.469182  -2584.460579
I-trans                              -2585.205729   0.809640  -2584.349802   0.122930   0.113173  -2584.472732  -2584.462975
IcisB-Ag                             -2732.062889   0.811622  -2731.203069   0.128446   0.117128  -2731.331515  -2731.320198
IcisB-bis_Ag                         -2732.064541   0.810613  -2731.205287   0.129893   0.118157  -2731.335180  -2731.323444
IcisB-ter_Ag                         -2732.062259   0.811394  -2731.202434   0.128870   0.117524  -2731.331305  -2731.319959
*************************************************************************************************************************
```

```
python3 -m goodvibes salen/*.log -f 100 -qs grimme
```

```
Entropic quasi-harmonic treatment: frequency cut-off value of 100.0 wavenumbers will be applied.
QS = Grimme: Using a mixture of RRHO and Free-rotor vibrational entropies.
REF: Grimme, S. Chem. Eur. J. 2012, 18, 9955-9964

Structure                                    E        ZPE            H        T.S     T.qh-S          G(T)       qh-G(T)
*************************************************************************************************************************
I-Ag                                 -2732.070316   0.811234  -2731.210792   0.128169   0.118908  -2731.338961  -2731.329700
I-cisB                               -2585.203482   0.809879  -2584.347323   0.121859   0.114178  -2584.469182  -2584.461501
I-trans                              -2585.205729   0.809640  -2584.349802   0.122930   0.114661  -2584.472732  -2584.464463
IcisB-Ag                             -2732.062889   0.811622  -2731.203069   0.128446   0.119212  -2731.331515  -2731.322282
IcisB-bis_Ag                         -2732.064541   0.810613  -2731.205287   0.129893   0.120023  -2731.335180  -2731.325310
IcisB-ter_Ag                         -2732.062259   0.811394  -2731.202434   0.128870   0.119341  -2731.331305  -2731.321775
*************************************************************************************************************************
```

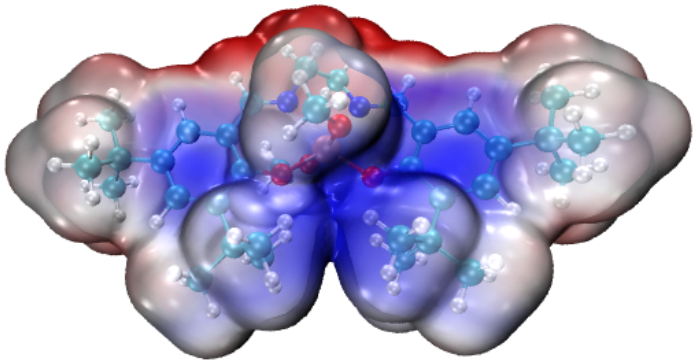

Figure S33: Molecular electrostatic potential surface (EPS) of **I** showing high electronic density areas (in blue) able to favour attractive electrostatic interactions with an Ag^+ atom.

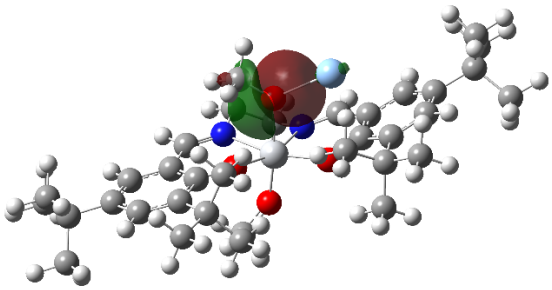

Natural $O_{(OMe)}$ filled lone pair orbital
LP $O_{(OMe)}$: $sp^{1.49}$
occupancy: 1.9

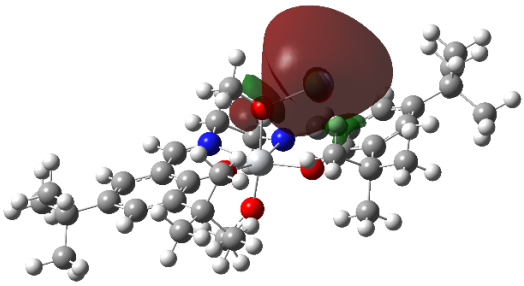

Natural Ag unfilled lone vacancy orbital
LV Ag: $sp^{0.03}d^{0.02}$
occupancy: 0.02

Figure S34: Selected natural orbital plots showing an orbital interaction (2nd order perturbation, ~ 10 kcal/mol) between the oxygen atom of the methoxy group and the Ag^+ atom in in ***trans*-I-Ag$^+$ (**data available at DOI: 10.14469/hpc/8745)

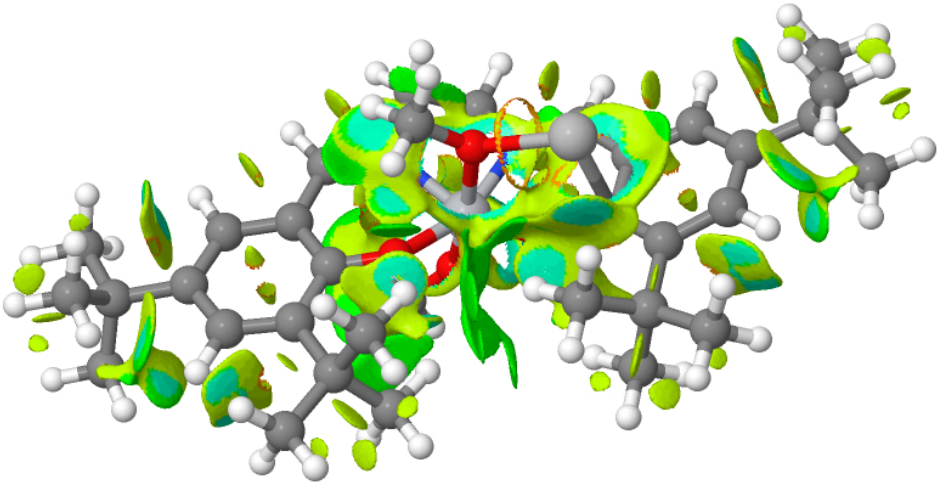

Figure S35: Non-Covalent Interactions (NCI) surfaces showing cation-Π interactions between Ag^+ and the phenolate moiety (see aforementioned details for parameters).

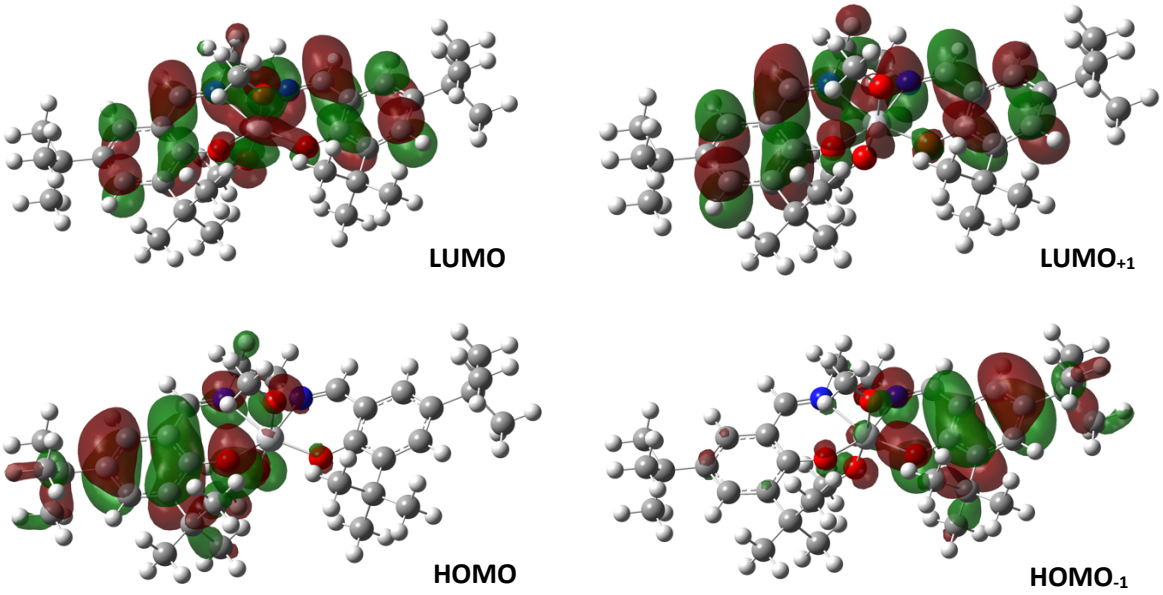

Figure S36: Selected molecular orbitals plots for **I** (isovalue = 0.02 a.u.).

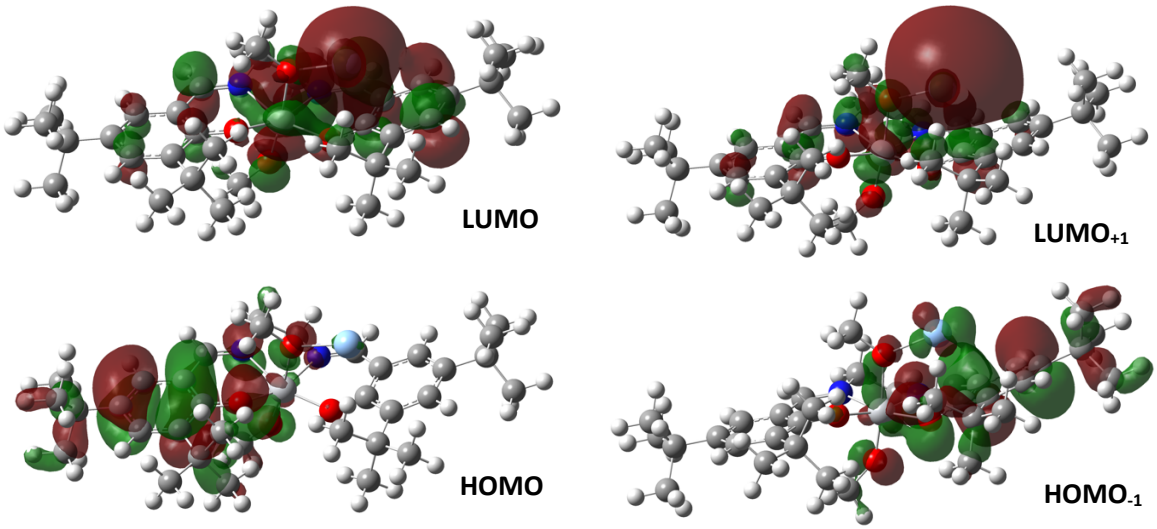

Figure S37: Selected molecular orbitals plots for **I-Ag**$^{+}$ (isovalue = 0.02 a.u.) showing electronic density distributed on one of the phenolate moieties of the salen ligand and the silver atom in HOMO$_{-1}$.

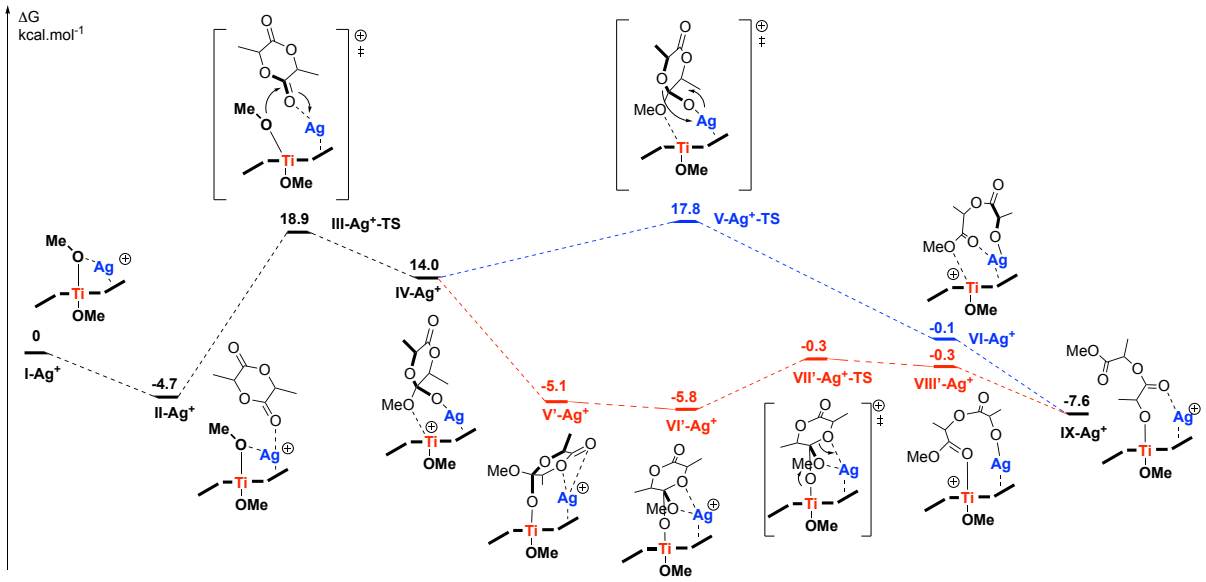

Figure S38: Potential energy surface (PES) corresponding to L-lactide opening (nucleophilic attack on *si* face) using ***trans*-I-Ag$^+$** (referred to as **I-Ag$^+$** for clarity), data available at DOI: 10.14469/hpc/8730.

Considering **I-Ag$^+$** as initiator, ring-opening of L-lactide (L-LA, *si* face) was investigated considering a well-studied coordination-insertion mechanism. One molecule of L-LA was found to favorably bind to the cationic silver atom of **I-Ag$^+$** leading to intermediate **II-Ag$^+$** ($\Delta\Delta G$ = -4.7 kcal/mol) featuring a suitable orientation of the monomer with regards to the methoxy ligand. This favors nucleophilic attack by the elongated Ti-OMe bond onto the lactide carbonyl via transition state **III-Ag$^+$-TS** at 18.9 kcal/mol on the potential energy surface (i.e energy barrier = 23.6 kcal.mol^{-1}). To some extent, the coordination of the Ag$^+$ provides an electrophilic assistance rendering the OMe group more labile and favoring nucleophilic attack.[26] The resulting intermediate **IV-Ag$^+$** features a tetrahedral anionic moiety coordinated to Ag$^+$ along with a cationic titanium center stabilized by the dative coordination of an oxygen atom of the methoxy group. Due to the hard and oxophilic nature of the titanium center, this intermediate rearranges to form the more stable intermediate **V'-Ag$^+$** where the anionic ligand is coordinated to Ti and the cationic charge localized on the silver atom. After free rotation of the anionic ligand along the Ti-O bond (**VI'-Ag$^+$**), the silver atom was found to be suitably positioned to favor ring-opening via transition state **VII'-Ag$^+$-TS** at on only -0.3 kcal/mol on the PES. As previously observed, it results intermediate **VIII'-Ag$^+$**, featuring an anionic alkoxide ligand coordinated to Ag$^+$ along with a cationic titanium center stabilized by the dative coordination of an ester oxygen atom. Migration of the anionic ligand to Ti leads to the stable intermediate **IX-Ag$^+$** ($\Delta\Delta G$ = -7.6 kcal/mol). Overall, such an *Ag-assisted Ti-mediated* L-LA ring-opening occurs with an overall energy barrier of 23.2 kcal/mol, in line with a reaction occurring at room temperature. Alternatively, ring opening of intermediate **IV-Ag$^+$** (i.e. without prior migration of the anionic ligand to Ti) has been found to occur via transition state **V-Ag-TS** at 17.8 kcal/mol on the PES, which also represents a possible pathway (blue path).

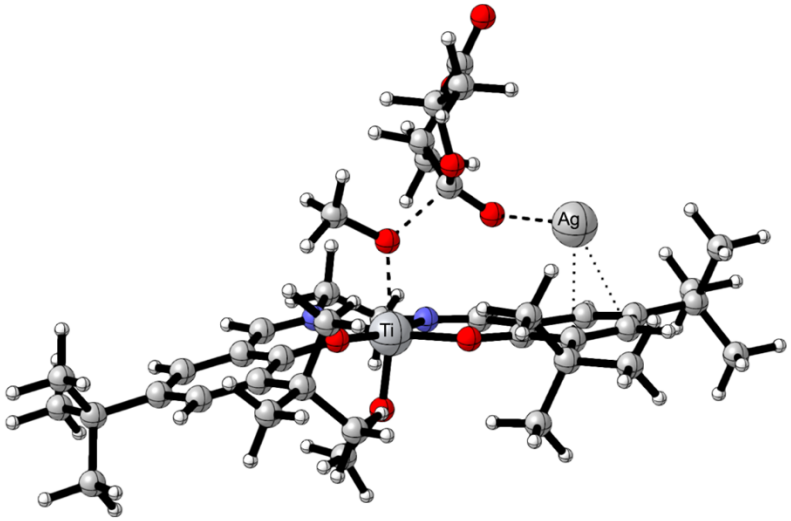

Figure S39: Optimised geometry of **III-Ag$^+$-TS** showing nucleophilic attack of the Ti-OMe to the carbonyl of L-LA coordinated to Ag$^+$ (data available at DOI: 10.14469/hpc/8734).

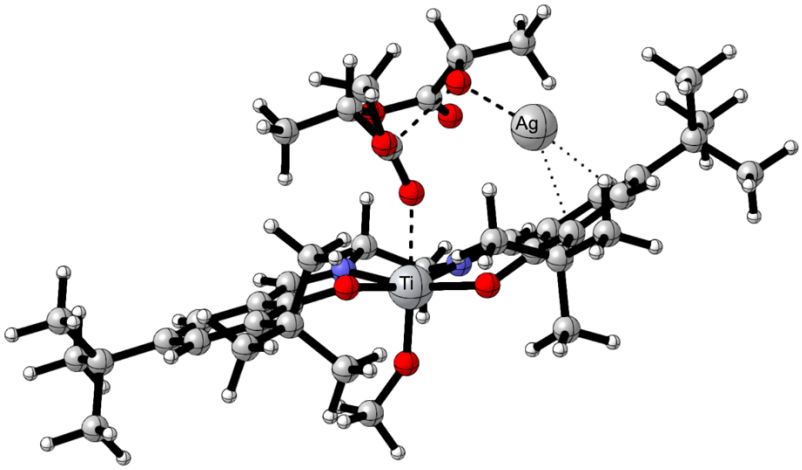

Figure S40: Optimised geometry of **VII'-Ag$^+$-TS** showing ring-opening of ligand coordinated to Ti along with interaction with Ag$^+$ (data available at DOI: 10.14469/hpc/8741).

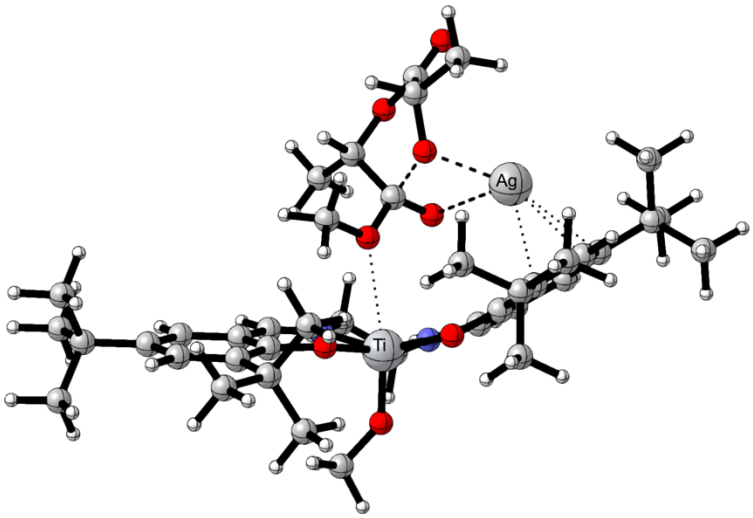

Figure S41: Optimised geometry of **V-Ag$^+$-TS** showing ring-opening of ligand coordinated to Ag$^+$ (data available at DOI: 10.14469/hpc/8736).

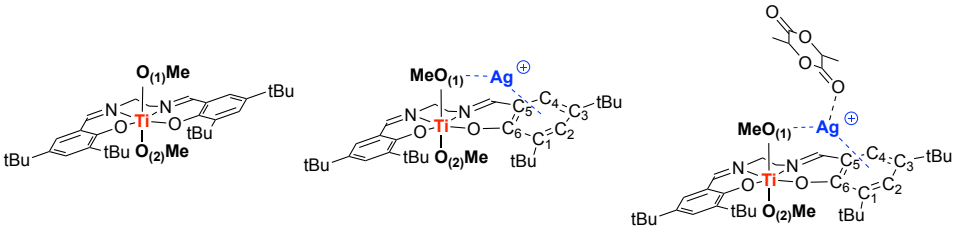

I ***trans*-I-Ag$^+$** **II-Ag$^+$**

Wiberg bond Index			
Ti-$O_{(1)}$	0.81	0.47	0.49
Ti-$O_{(2)}$	0.85	1.01	1.00
$O_{(1)}$-Ag	--	0.10	0.06
Ag-$O_{(c=o)}$	--	--	0.06
NBO charges			
Ag	--	+ 0.94	+ 0.92
$O_{(1)}$	-0.73	-0. 92	-0.91
$O_{(2)}$	-0.72	-0.66	-0.66

Figure S42: Selected NBO analysis data showing a lower Wiberg bond index and higher negative charge on $O_{(1)}$ atom in heterobimetallic species (i.e. **I-Ag$^+$** and **II-Ag$^+$** as per Figure S35) compared to **I**, suggesting a higher nucleophilicity of the OMe group, data available at DOI: 10.14469/hpc/8744.

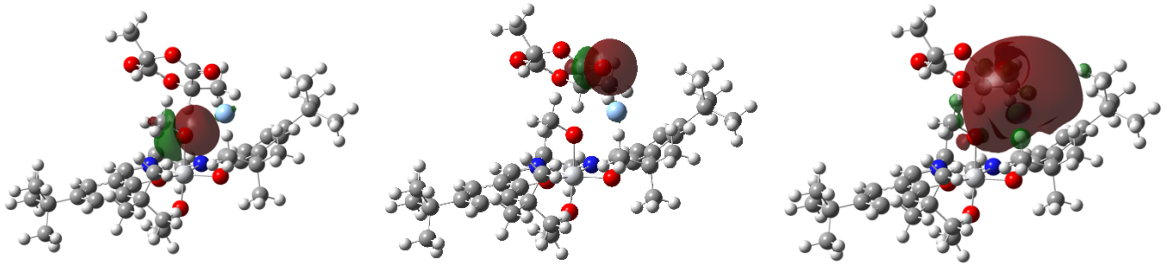

Natural O(OMe) filled lone pair
LP O(OMe): $sp^{1.28}$
Occupancy: 1.9

Natural $O_{(C=O)}$ filled lone pair
LP $O_{(C=O)}$: $sp^{1.49}$
Occupancy: 1.96

Natural Ag unfilled lone vacancy
LV Ag: $sp^{0.01}d^{0.01}$
Occupancy: 0.09

Figure S43: Selected natural orbital plots showing orbital interactions (2nd order perturbation) in in **II-Ag$^+$** between i) the oxygen atom of the methoxy group and the Ag$^+$ cation (LP $O_{(OMe)}$ → LV Ag = 10.7 kcal.mol^{-1}) and, ii) the oxygen atom of lactide carbonyl and the Ag$^+$ cation (LP $O_{(C=O)}$ → LV Ag = 8.50 kcal.mol^{-1}), data available at DOI: 10.14469/hpc/8744.

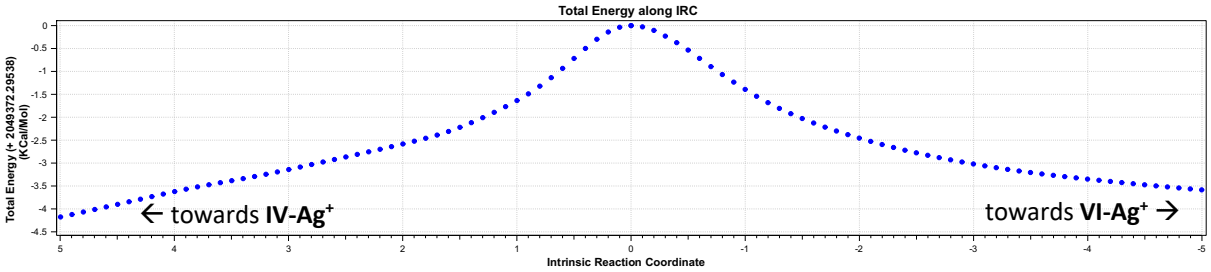

Figure S44: Intrinsic Reaction Coordinate (IRC) for **V-Ag$^+$-TS** (data available at DOI: 10.14469/hpc/8736).

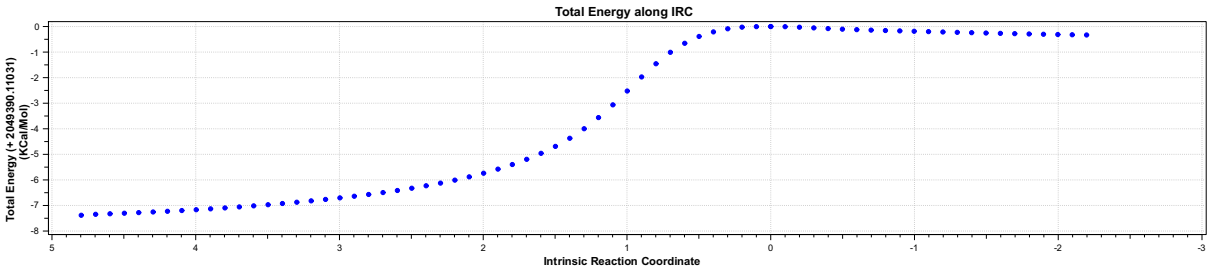

Figure S45: Intrinsic Reaction Coordinate (IRC) for **VII'-Ag$^+$-TS** (data available at DOI: 10.14469/hpc/8741).

References:

1. M. D. Wilkinson, M. Dumontier, I. J. Aalbersberg, G. Appleton, M. Axton, A. Baak, N. Blomberg, J.-W. Boiten, L. B. da Silva Santos, P. E. Bourne, J. Bouwman, A. J. Brookes, T. Clark, M. Crosas, I. Dillo, O. Dumon, S. Edmunds, C. T. Evelo, R. Finkers, A. Gonzalez-Beltran, A. J. G. Gray, P. Groth, C. Goble, J. S. Grethe, J. Heringa, P. A. C. 't Hoen, R. Hooft, T. Kuhn, R. Kok, J. Kok, S. J. Lusher, M. E. Martone, A. Mons, A. L. Packer, B. Persson, P. Rocca-Serra, M. Roos, R. van Schaik, S.-A. Sansone, E. Schultes, T. Sengstag, T. Slater, G. Strawn, M. A. Swertz, M. Thompson, J. van der Lei, E. van Mulligen, J. Velterop, A. Waagmeester, P. Wittenburg, K. Wolstencroft, J. Zhao and B. Mons, *Sci. Data*, 2016, **3**, 160018.

2. A. Thevenon, A. Cyriac, D. Myers, A. J. P. White, C. B. Durr and C. K. Williams, *J. Am. Chem. Soc.*, 2018, **140**, 6893-6903.

3. X. Wang, O. Shyshov, M. Hanževački, C. M. Jäger and M. von Delius, *J. Am. Chem. Soc.*, 2019, **141**, 8868-8876.

4. M. E. Payne and S. M. Grayson, *J Vis Exp*, 2018, e57174.

5. C. K. Gregson, I. J. Blackmore, V. C. Gibson, N. J. Long, E. L. Marshall and A. J. White, *Dalton Trans*, 2006, 3134-3140.

6. A. Barba, S. Dominguez, C. Cobas, D. P. Martinsen, C. Romain, H. S. Rzepa and F. Seoane, *ACS Omega*, 2019, **4**, 3280-3286.

7. M. Save, M. Schappacher and A. Soum, *Macromol. Chem. Phys.*, 2002, **203**, 889-899.

8. M. J. Frisch, G. W. Trucks, H. B. Schlegel, G. E. Scuseria, M. A. Robb, J. R. Cheeseman, G. Scalmani, V. Barone, G. A. Petersson, H. Nakatsuji, X. Li, M. Caricato, A. V. Marenich, J. Bloino, B. G. Janesko, R. Gomperts, B. Mennucci, H. P. Hratchian, J. V. Ortiz, A. F. Izmaylov, J. L. Sonnenberg, Williams, F. Ding, F. Lipparini, F. Egidi, J. Goings, B. Peng, A. Petrone, T. Henderson, D. Ranasinghe, V. G. Zakrzewski, J. Gao, N. Rega, G. Zheng, W. Liang, M. Hada, M. Ehara, K. Toyota, R. Fukuda, J. Hasegawa, M. Ishida, T. Nakajima, Y. Honda, O. Kitao, H. Nakai, T. Vreven, K. Throssell, J. A. Montgomery Jr., J. E. Peralta, F. Ogliaro, M. J. Bearpark, J. J. Heyd, E. N. Brothers, K. N. Kudin, V. N. Staroverov, T. A. Keith, R. Kobayashi, J. Normand, K. Raghavachari, A. P. Rendell, J. C. Burant, S. S. Iyengar, J. Tomasi, M. Cossi, J. M. Millam, M. Klene, C. Adamo, R. Cammi, J. W. Ochterski, R. L. Martin, K. Morokuma, O. Farkas, J. B. Foresman and D. J. Fox, *Journal*, 2016.

9. B. P. Pritchard, D. Altarawy, B. Didier, T. D. Gibson and T. L. Windus, *J. Chem. Inf. Model.*, 2019, **59**, 4814-4820.

10. C. Y. Legault, *CYLview20, Université de Sherbrooke, http://www.cylview.org*, 2020.

11. T. Lu and F. Chen, *J. Comput. Chem.*, 2012, **33**, 580-592.

12. G. Luchini, J. Alegre-Requena, I. Funes-Ardoiz and R. Paton, *F1000Research*, 2020, **9**.

13. E. D. Glendening, J. K. Badenhoop, A. E. Reed, J. E. Carpenter, J. A. Bohmann, C. M. Morales, C. R. Landis and F. Weinhold, *NBO 6.0, Theoretical Chemistry Institute, University of Wisconsin, Madison, WI, http://nbo6.chem.wisc.edu/*, 2013.

14. M. F. Ibad, A. Schulz and A. Villinger, *Organometallics*, 2019, **38**, 1445-1458.

15. I. Kim, Y. S. Ha, D. F. Zhang, C.-S. Ha and U. Lee, *Macromol. Rapid Commun.*, 2004, **25**, 1319-1323.

16. Y. N. Belokon, W. Clegg, R. W. Harrington, C. Young and M. North, *Tetrahedron*, 2007, **63**, 5287-5299.

17. (a) M. Nayak, S. Sarkar, S. Hazra, H. A. Sparkes, J. A. K. Howard and S. Mohanta, *CrystEngComm*, 2011, **13**, 124-132; (b) N. Şenyüz, B. Yılmaz, H. Batı, E. Bozkurt and O. Büyükgüngör, *Spectrochim. Acta A Mol. Biomol. Spectrosc.*, 2013, **101**, 167-171; (c) A. Biswas, S. Mondal, L. Mandal, A. Jana, P. Chakraborty and S. Mohanta, *Inorg. Chim. Acta*, 2014, **414**, 199-209.

18. S. S. Batsanov, *Inorganic Materials*, 2001, **37**, 871-885.

19. (a) S. Mandal, N. Hari, S. Mondal and S. Mohanta, *ChemistrySelect*, 2018, **3**, 9610-9616; (b) K. Helttunen, N. Moridi, P. Shahgaldian and M. Nissinen, *Org. Biomol. Chem.*, 2012, **10**, 2019-2025.

20. A. Ferretti, M. d'Ischia and G. Prampolini, *J. Phys. Chem. A*, 2020, **124**, 3445-3459.

21. S. Bellemin-Laponnaz and S. Dagorne, in *PATAI'S Chemistry of Functional Groups*, 2012.

22. (a) H. Chen, P. S. White and M. R. Gagné, *Organometallics*, 1998, **17**, 5358-5366; (b) R. K. Gurung, C. D. McMillen, W. L. Jarrett and A. A. Holder, *Inorg. Chim. Acta*, 2020, **505**, 119496.

23. (a) G. Gilli, D. W. J. Cruickshank, R. L. Beddoes and O. S. Mills, *Act. Cryst. B*, 1972, **28**, 1889-1893; (b) T. Repo, M. Klinga, M. Leskelä, P. Pietikäinen and G. Brunow, *Act. Cryst. C*, 1996, **52**, 2742-2745.
24. C. Floriani, E. Solari, F. Corazza, A. Chiesi-Villa and C. Guastini, *Angew. Chem. Ed. Int.*, 1989, **28**, 64-66.
25. (a) A. J. Nielson, S. G. Telfer and J. M. Waters, *Polyhedron*, 2012, **33**, 97-106; (b) T. Masanobu, *Bull. Chem. Soc. Jpn.*, 2001, **74**, 2101-2105; (c) F. Franceschi, E. Gallo, E. Solari, C. Floriani, A. Chiesi-Villa, C. Rizzoli, N. Re and A. Sgamellotti, *Chem. Eur. J.*, 1996, **2**, 1466-1476.
26. C. Morpain and J. J. Perie, *Tetrahedron*, 1985, **41**, 317-328.